HAL
open science

Predicting the 3D fatigue crack growth rate of short cracks using multimodal data via Bayesian network: in-situ experiments and crystal plasticity simulations

Andrea Rovinelli, Michael Sangid, Henry Proudhon, Yoann Guilhem, Ricardo A. Lebensohn, Wolfgang Ludwig

To cite this version:

Andrea Rovinelli, Michael Sangid, Henry Proudhon, Yoann Guilhem, Ricardo A. Lebensohn, et al.. Predicting the 3D fatigue crack growth rate of short cracks using multimodal data via Bayesian network: in-situ experiments and crystal plasticity simulations. Journal of the Mechanics and Physics of Solids, 2018, 115, pp.208-229. 10.1016/j.jmps.2018.03.007 . hal-01729179

HAL Id: hal-01729179

https://hal.science/hal-01729179v1

Submitted on 22 Mar 2018

HAL is a multi-disciplinary open access archive for the deposit and dissemination of scientific research documents, whether they are published or not. The documents may come from teaching and research institutions in France or abroad, or from public or private research centers.

L'archive ouverte pluridisciplinaire **HAL**, est destinée au dépôt et à la diffusion de documents scientifiques de niveau recherche, publiés ou non, émanant des établissements d'enseignement et de recherche français ou étrangers, des laboratoires publics ou privés.

For submission to the Journal of Mechanics and Physics of Solids, November 2017

Predicting the 3D Fatigue Crack Growth Rate of Short Cracks Using Multimodal Data via Bayesian Network: in-situ Experiments and Crystal Plasticity Simulations

Andrea Rovinelli[1], Michael D. Sangid[1,*], Henry Proudhon[2], Yoann Guilhem[3], Ricardo A. Lebensohn[4], Wolfgang Ludwig[5]

[1] School of Aeronautics and Astronautics, Purdue University, 701 W. Stadium Ave, West Lafayette, IN 47907, USA
[2] MINES ParisTech, PSL Research University, MAT - Centre des matériaux, CNRS UMR 7633, BP 87 91003 Evry, France
[3] Laboratoire de Mécanique et Technologie (LMT), ENS Paris-Saclay/CNRS/Université Paris-Saclay, 61 avenue du Président Wilson, F-94235 Cachan Cedex, France
[4] Theoretical Division, Los Alamos National Laboratory, Los Alamos, NM 87545, USA
[5] University of Lyon, INSA Lyon, MATEIS, UMR 5510 CNRS, F-69621, LYON, France
* Corresponding Author, e-mail address: msangid@purdue.edu

Abstract

Small crack (SC) propagation accounts for most of the fatigue life of engineering structures subject to high cycle fatigue loading conditions. Determining the fatigue crack growth rate of SCs propagating into polycrystalline engineering alloys is critical to improving fatigue life predictions, thus lowering cost and increasing safety. In this work, cycle-by-cycle data of a SC propagating in a beta metastable titanium alloy is available via phase and diffraction contrast tomography. Crystal plasticity simulations are used to supplement experimental data regarding the micromechanical fields ahead of the crack tip. Experimental and numerical results are combined into a multimodal dataset and sampled utilizing a non-local data mining procedure. Furthermore, to capture the propensity of body-centered cubic metals to deform according to the pencil-glide model, a non-local driving force is postulated. The proposed driving force serves as the basis to construct a data-driven probabilistic SC propagation framework using Bayesian networks as building blocks. The spatial correlation between the postulated driving force and experimental observations is obtained by analyzing the results of the SC propagation Bayesian framework. Results show that the above correlation increases proportionally to the distance from the crack front until the edge of the plastic zone. Moreover, the predictions of the propagation framework show good agreement with experimental observations. Finally, we studied the interaction of a SC with grain boundaries (GBs) utilizing various slip transmission criteria, revealing the tendency of a SC to cross a GB by propagating along the slip directions minimizing the residual Burgers vector with the GB.

Keywords: A small crack propagation; B crystal plasticity; B polycrystalline material; C nondestructive evaluation; machine learning;

Uncommon abbreviations[£]

Highlights (mandatory, 3-5 bullets, 85 characters with spaces)

- In BCC materials, small cracks propagate accordingly to the pencil-glide model.
- A non-local, direction dependent data mining procedure captures crack mechanics.
- The proposed non-local driving force adequately reproduces 3D experimental results.
- Small cracks overcome grain boundaries by minimizing the residual Burgers vector.

[£] 3D x-ray tomography for small crack and microstructure (3DXTSM), Bayesian network (BN), driving force (DF), data mining procedure (DMP), fatigue indicator parameter (FIP), FnF (fail /not-fail), failing slip direction (FSD), growth rate (GR), non-failing slip direction (NFSD), normalized mutual information (NMI), mutual information (MI), small crack (SC).

Graphical Abstract

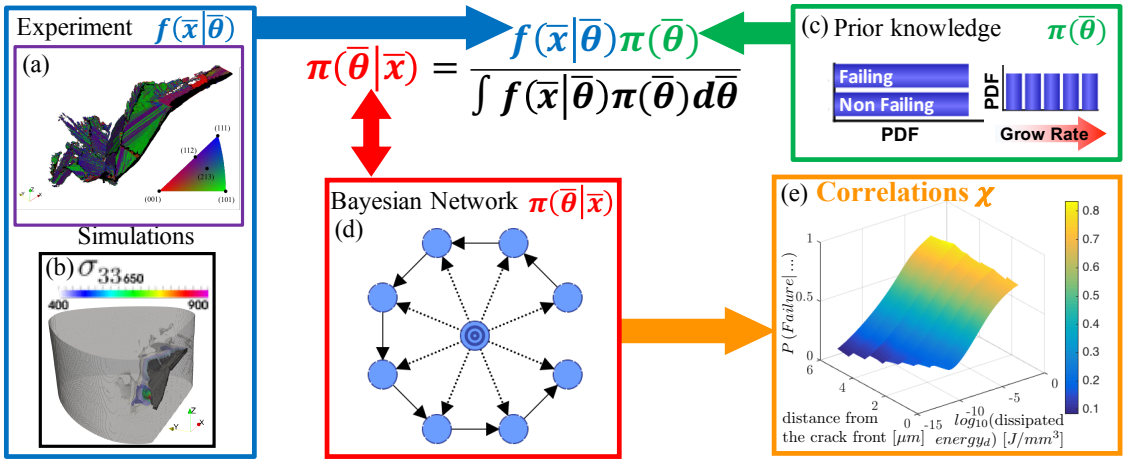

1 Introduction

The fatigue crack growth rate (FCGR) of a long crack in high cycle fatigue regime can be predicted utilizing the Paris law (Paris et al., 1961). However, traditional fracture mechanics theory does not provide accurate predictions when the crack's length is comparable to the microstructural length scale. The above regime is referred to as stage I, and cracks are classified as small cracks (SCs) within this regime. In fact, for a SC the material cannot be considered homogeneous because microstructural features in the proximity of the crack front influence the spatial distribution of micromechanical fields (i.e. stress, strain, displacement, etc., Rovinelli et al., 2015). The result of the SC interacting with the surrounding microstructure is the extreme scatter of the FCGR observed in stage I (Bray et al., 2001; Davidson et al., 2003). Furthermore, it is well established that more than 60% of the lifespan of an engineering structure or component subject to high cycle fatigue is associated with the propagation of SCs (Schijve, 2009). Hence, understanding the small crack driving force of engineering alloys is critical to obtain reliable life predictions to improve both design and maintenance operations. This goal has not been achieved yet because of: (i) the lack of data at the appropriate length scale and (ii) to the complex interactions between a SC and microstructure features. In this work, experimental data collected via synchrotron imaging and results of crystal plasticity simulations are used to investigate the behavior of a SC propagating within a beta metastable titanium alloy.

To explain the serrated surface of a SC, Neumann proposed the coarse-slip model, which is based on the alternate activation of two different slip planes (Neumann, 1974a, 1974b, 1969). Vehoff and Neumann (1979) experimentally observed SCs propagating accordingly to the coarse-slip model in both face and body centered cubic (FCC and BCC, respectively) single-crystals. However, recent high-resolution experimental observations by Schäf et al. (2013, 2011) show that in polycrystalline aggregates, SCs do not always propagate conforming to the model proposed by Neumann.

In general, plastic deformation in FCC metals and alloys can be described as a deck of cards subject to shear loading. In the card-glide model, both the direction and plane of slip are prescribed. The card represents a slip plane (i.e. any of the $\{111\}$) and the glide direction is one of the available slip directions (i.e. any $\langle 110 \rangle$). Taylor and Elam (1926) observed card-glide in BCC materials, but only when a crystal is subject to homogeneous shear. For more complex loading conditions, they identified deformations aligned with slip directions but not always related to crystallographic slip planes. They hypothesized that BCC alloys deform as a large bundle of rods slipping relative to each other, conjecturing that atoms stick together along a certain crystallographic direction (i.e. $\langle 111 \rangle$). Hence, the slip plane is not necessarily crystallographic and may be any plane embedding the slip direction. Since its elicitation, the latter deformation mechanism, referred to as pencil-glide, has proven useful in predicting plastic deformation and texture evolution of polycrystalline BCC metals (Gilormini et al., 1988; Kocks, 1970). Hence, to predict the FCGR in BCC metals, a small crack propagation framework based upon the pencil-glide model is proposed.

Much work has been done in assessing the correlation between micromechanical fields, crack nucleation events and microstructure features for FCC metals. Hochhalter et al. (2011)

investigated the ability of different fatigue indicators parameters (FIPs) to predict crack nucleation sites, observing no substantial difference between the analyzed FIPs. Yeratapally et al. (2016) and Cerrone et al. (2015) found that spatial regions exhibiting strong elastic anisotropy and relevant localized plasticity are favorable sites for crack nucleation in Nickel-based superalloys. Based on the work of Fatemi and Socie (1988), Castelluccio and McDowell (2012) proposed a FIP based on cyclic plastic strain accumulation and the opening stress on the critical slip plane. The above FIP is known as the Fatemi-Socie FIP and has been correlated qualitatively with the crack tip opening displacement and the variability of the FCGR in FCC alloys (Castelluccio and McDowell, 2014, 2012).

However, fewer efforts have been made in trying to replicate the SC path. Musinski and McDowell (2016) modified the Fatemi-Socie FIP to account for the interaction between SCs and GBs, calibrated the model against 1D experimental data, and used it to simulate the temporal and spatial evolution of a 3D SC. The model showed convergence to linear elastic fracture mechanics, but a direct comparison with 3D data was not performed due to the lack of experimental data. Li et al. (2014) and Proudhon et al. (2017) were among the first in trying to reproduce an experimentally observed SC utilizing a FIP as the driving force for the crack advancement. Data was collected utilizing a technique known as 3D x-ray tomography for small crack and microstructure (3DXTSM, Herbig et al., 2011), which provides high-resolution images of SCs propagating into a polycrystalline aggregate. When comparing simulation results with experimental observations, they found a high-sensitivity of the simulated crack path with respect to the imposed boundary conditions and emphasized the need for a FIP threshold value for crack propagation to accurately reproduce the FCGR (Proudhon et al., 2015). Rovinelli et al. (2017) investigated the correlation between several FIPs and the experimentally observed FCGR in a BCC alloy subjected to high-cycle fatigue loading conditions. Results showed that all the scrutinized FIPs behave similarly and exhibit low predictive performance. In this work, to predict the FCGR in BCC alloys, a non-local driving force is proposed, computed via crystal plasticity simulations, and spatially correlated with experimental observations.

Probabilistic tools are used to identify relevant correlations and to quantify uncertainty. The major drawback of the above kind of analysis is the amount of data required to obtain trustable results. The classic Bayesian approach coupled with Markov chain Monte Carlo methods (Metropolis et al., 1953; Metropolis and Ulam, 1949) provides a means to overcome the shortage of experimental data while calculating the posterior probability distribution. In this methodology, the likelihood function and a priori belief are directly encoded in the model by selecting appropriate distributions. This method has proven to be effective to quantify uncertainties in many fields, including fatigue (Yeratapally et al., 2017). However, it is computationally expensive and is predominantly based on expert knowledge. The latter means that suitable distributions (e.g. normal, beta, gamma, etc.) and their parameters (e.g. variance, mean, etc.) need to be elicited not only for the prior distributions but also for the likelihood function.

If the likelihood function can be estimated from the data, then the computational cost associated with the classic Bayesian approach can be significantly reduced by means of a Bayesian network (Pearl, 1985). Moreover, a Bayesian network possesses the following features: (i) is non-parametric, (ii) allows for omnidirectional inferences, and (iii) permits extraction of correlations embedded in the model parameters. In this work, experimental data

and results of crystal plasticity simulations are combined into a multimodal dataset, which is used to build a data-driven Bayesian network framework. The latter is utilized to evaluate the predictive performance of the proposed driving force and to compute correlations.

To identify the correlation between micromechanical fields and the observed FCGR, the FCGR needs to be reconstructed from a series of static experimental images. For long cracks, the crack front is assumed to be elliptical and flat, and the FCGR is estimated assuming radial propagation from a unique crack center. To account for the tortuous nature of a SC, variations of the standard procedure have been utilized by different authors (Herbig et al., 2011; Spear et al., 2014). However, the above procedures provide an adequate estimation of the FCGR only when analyzing a well-behaved SC (e.g. no bifurcations and an almost ellipsoidal front). To better estimate the FCGR of a tortuous crack a reconstruction procedure based on the pencil-glide model is presented (Kocks, 1970).

High-resolution imaging and reconstruction techniques allow for further investigation of propagation mechanisms of SCs. Zhang and Edwards (1992) studied the interactions between SCs and GBs. They stated that the initiation of plasticity in the adjacent grain is one of the necessary condition required by a SC to overcome a GB. The above suggests that slip transmission criteria may be utilized to predict which path the crack will follow when crossing a GB. Following this idea, Zhai et al. (2005, 2000) proposed a geometric model for SC propagation based on the minimum twist angle between the crack plane and the available slip planes in the adjacent grain. In the Zhai model, the minimum twist angle is proportional to the deceleration exhibited by a SC when imping upon a GB. Furthermore, if all the slip planes are strongly misaligned, then the crack propagates in the adjacent grain on two separate slip planes to minimize the energy required to rupture the GB. Schäf et al. (2013, 2011) experimentally investigated the behavior of a SC when crossing a GB in 3D and viewed this behavior via a technique that combines focused ion beam cross sectioning and scanning electron microscope imaging. They found that the Zhai model is qualitatively correct for FCC, but it does not always hold for BCC materials. Studies of this kind investigated the surface of the material, or a thin layer of it, always assuming the GB is straight and perpendicular to the analyzed surface. Results of 3DXTSM provide unique insights at the appropriate length scale on the behavior of a SC interacting with a GB without requiring strong assumption on the topology of the microstructure. Therefore, to investigate the behavior of a SC when crossing a GB, several slip transmission criteria are applied to the available dataset and compared with experimental evidence.

The aims of this article are four-fold: (i) to present a data-driven probabilistic framework to predict the FCGR; (ii) to propose a non-local driving force for polycrystalline BCC metals; (iii) to quantify the spatial correlation between the postulated driving force and the observed FCGR; and (iv) to investigate the ability of several slip transmission criteria to predict the crack path when crossing a GB. The remainder of the article is organized as follows. Section 2 is divided into 4 subsections: Section 2.1 is a brief overview of the probabilistic, data-driven small crack growth propagation framework and the core ideas behind it; Section 2.2 presents all the experimental and numerical tools required to generate the data used by the framework above; Section 2.3 explains the implementation of the proposed framework, how to evaluate its performance, and how to quantify correlations embedded in the data; Section 2.4 is dedicated

to the investigated slip transmission criteria. Section 3 contains results and discussions. Specifically: Section 3.1 presents relevant results of the utilized numerical tools; Section 3.2 is focused on the outcomes of the proposed probabilistic framework and their significance; Section 3.3 is dedicated to the interaction between SCs and GBs. Section 4 summarizes the scientific relevance of this article.

2 Methodology and tools

2.1 Overview of the small crack growth propagation framework

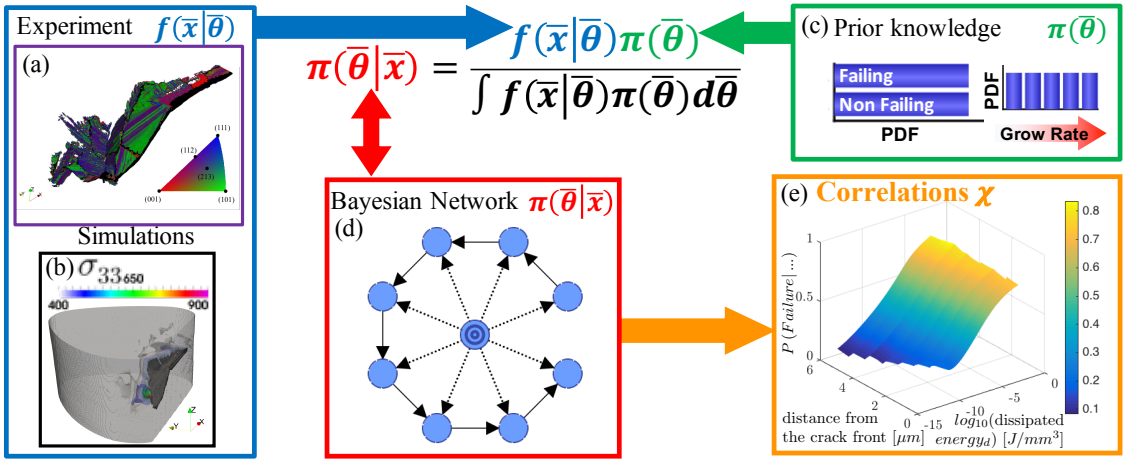

Figure 1. Schematic representation of the non-local, data-driven probabilistic small crack propagation framework. (a) Experiment and (b) simulations results are combined into a multimodal dataset from which the likelihood function can be estimated. (c) Uniform prior distributions are selected to investigate the correlations embedded in the data. Bayesian networks are utilized as a tool to compute (d) the posterior probability via Bayes' theorem and to quantify (e) the correlations embedded in the data.

Figure 1 is a schematic depicting the proposed non-local, data-driven probabilistic small crack propagation framework. Bayes' theorem (Equation 1) is the core of the framework. It provides a means to compute the posterior probability $\pi(\bar{\theta}|\bar{x})$ of an event $\bar{\theta}$ happening when observing a set of evidence $\bar{x}$. In this work, $\bar{\theta}$ represents the probability of failure of a slip direction or the FCGR, and $\bar{x}$ represents the computed values of the proposed non-local driving force.

$$\pi(\bar{\theta}|\bar{x}) = \frac{f(\bar{x}|\bar{\theta})\pi(\bar{\theta})}{\int f(\bar{x}|\bar{\theta})\pi(\bar{\theta})d\bar{\theta}} \qquad \textit{Equation 1}$$

Two other quantities are required to compute the posterior probability: (i) the likelihood function (i.e. $f(\bar{x}|\bar{\theta})$) and (ii) the distribution of the prior probability (i.e. $\pi(\bar{\theta})$). The likelihood function is computed combining experiment and simulation results into a multimodal dataset (Figure 1 (a) and (b)). Specifically, experimental data has been collected via 3DXTSM methodology (Herbig et al., 2011) and crystal plasticity simulations are used to compute micromechanical fields (Rovinelli et al., 2017b) not recorded during the experiment. The distribution of prior probabilities is assumed uniform (Figure 1 (c)) to minimize the bias that may be present in the dataset. Subsequently, we utilize Bayesian networks to build the probabilistic models describing the SC propagation problem (Figure 1 (d)). Once the model is established, the posterior probability can be evaluated and correlations between the proposed driving force and experimental observations can be quantified (Figure 1 (e)). For these purposes, an off-the-shelf machine learning Bayesian network software is utilized (i.e. Bayesialab).

2.2 Methods

Some procedure utilized in this work, such as the voxelization of the crack surface, the identification of the crack front, and the crack segmentation procedure, have been discussed in (Rovinelli et al., 2017b) and for brevity will not be reported here. However, the experimental methodology and simulations setup are briefly described to ensure this work is self-contained.

2.2.1 Experiment

The experimental technique utilized in this work to obtain a high-fidelity reconstruction of a small crack growing into a specimen is 3DXTSM (Herbig et al., 2011). The experiment has been performed at the European Synchrotron Radiation Facility at beamline ID-19, and the material investigated is a beta-metastable titanium alloy, commercially known as VST-55531. To obtain a coarse grain microstructure, which is required for optimal 3DXTSM results, the sample was solution annealed at 843 ℃ for 2 hours under vacuum and then air cooled. Electron backscatter diffraction scans show a full beta microstructure with a mean grain size of $65\ \mu m$ after recrystallization (Herbig et al., 2011).

The steps required by 3DXTSM are the following: (i) one initial diffraction contrast tomography to record the actual microstructure's topology and grain orientation and (ii) one phase contrast tomography every N fatigue loading cycles to record the current crack topology. In this experiment, $N = 1000$ until cycle 110k. Subsequently, $N = 500$ has been adopted to compensate for the increased FCGR. Moreover, the pixel size is $1.4\ \mu m$ and $0.7\ \mu m$ for diffraction contrast tomography and phase contrast tomography, respectively. The design of the fatigue loading frame (Buffiere et al., 2006) allows the test to be performed in-situ without the need to remove the sample from the load frame for tomography characterization.

2.2.2 Simulations

As described in (Rovinelli et al., 2017b), the simulations setup aims to mimic the experimental loading conditions to compute the micromechanical fields. The computational framework utilized in this work is a custom, parallel implementation of the small-strain, elasto-viscoplastic FFT-based crystal plasticity solver (CP-FFT) proposed by Lebensohn et al. (2012). CP-FFT is a more efficient alternative to solve the same problem with standard CP-Finite Elements (CP-FEM). A direct comparison between CP-FFT and CP-FEM predictions for configurations similar to the ones involved in the present analysis, corresponding to the determination of stress and strain fields and slip activity near a crack tip, was conducted and reported elsewhere, showing good agreement between the micromechanical fields obtained with both formulations (Rovinelli et al., 2017a). Equation 2 represents the adopted Hutchinson-type flow rule (Hutchinson, 1977) and Equations 3-5 describe the Harren-type hardening law (Harren et al., 1989). The latter has been modified to account for the experimentally observed cyclic softening behavior (Rovinelli et al., 2017b).

$$\dot{\gamma}^{\alpha} = \dot{\gamma}_0 \left(\frac{|\tau^{\alpha}|}{g^{\alpha}} \right)^n sign(\tau^{\alpha})$$ *Equation 2*

$$\dot{g}^{\alpha} = -\sum_{\beta=1}^{N} H^{\alpha\beta} |\dot{\gamma}^{\beta}| = -\sum_{\beta=1}^{N} q^{\alpha\beta} h^{\beta} |\dot{\gamma}^{\beta}|$$ *Equation 3*

$$h^{\alpha} = h_s^{\alpha} + sech^2 \left[\left(\frac{h_s^{\alpha} - h_0^{\alpha}}{\tau_s^{\alpha} - \tau_0^{\alpha}} \right) \Gamma \right] (h_s^{\alpha} - h_0^{\alpha})$$ *Equation 4*

$$\Gamma = \int_0^T \sum_{\alpha=1}^{N} |\dot{\gamma}^{\alpha}| dt$$ *Equation 5*

where α, β are the slip system indices (here all three families $\{110\}$,$\{112\}$,$\{123\}$ are included, hence N=48), τ^{α} is the resolved shear stress, g^{α} is the critical resolved shear stress, $\dot{\gamma}^{\alpha}$ is the plastic shear strain rate, $\dot{\gamma}_0$ is a scaling constant, $h_0^{\alpha}, h_s^{\alpha}$, are respectively single slip initial and saturation hardening rate, h^{α} is a variable scaling the effect of slip rate on the update of the critical resolved shear stress, $\Delta\tau^{\alpha} = \tau_s^{\alpha} - \tau_0^{\alpha}$ is the maximum allowable variation of the initial critical resolved shear stress, $q^{\alpha\beta}$ is a parameter representing self and latent hardening (q=1 if $\alpha = \beta$, 1.4 otherwise), Γ is the accumulated total plastic shear at an integration point, and $\dot{g}^{\alpha}$ defines the variation of the critical resolved shear stress.

Table 1 Summary of elastic and plastic constants utilized for the simulations.

Hardening parameter			Elastic Constants	
$\dot{\gamma}_0$ $[s^{-1}]$	2.5E-06		C_{1111} [GPa]	167
n	10		C_{1212} [GPa]	115
τ_0^{α} [MPa]	50		C_{2323} [GPa]	44
τ_s^{α} [MPa]	0			
h_o^{α} [MPa]	500			
h_s^{α} [MPa]	0			
g_0^{α} [MPa] {110} and {112}	405			
g_0^{α} [MPa] {123}	415			

Elastic constants have been selected from the literature (Fréour et al., 2011). The voxel size of the CP-FFT simulations is $1.4\ \mu m$, which is the same utilized for the diffraction contrast tomography scan.

Results obtained via 3DXTSM serve as input to the CP-FFT simulations. Each simulation consists of 100 fatigue loading cycles recording results three times per decade (i.e. cycle

1,2,5,10,20,50,100). Rovinelli et al. (2015) showed that the spatial distribution of FIPs in the proximity of the crack tip does not change with increased loading cycles. Therefore, only data collected at cycle 1 of each simulation will be used for the data analysis. Moreover, to avoid bias when computing correlations between the proposed driving force and experimental observations, the crack is not allowed to propagate. Each phase contrast tomography scan provides the geometry of the crack for one simulation.

2.2.3 Slip direction based modeling tools

2.2.3.1 3D small fatigue crack growth rate reconstruction

The procedure to reconstruct the observed FCGR relies on the premise that during the early stages of propagation (i.e. when the crack front encompasses only a few grains), the direction of propagation aligns with one of the available slip directions. In case of ambiguity, the optimal path is chosen as the one exhibiting the highest FCGR. Specifically, at each crack front location, all the available slip directions are followed for a predetermined length, $l_0 = 6.3\ \mu m$ while recording information of the nearest crack surface element. The reason for choosing the above value of l_0 is further discussed in Section 3.1. Moreover, the maximum orthogonal distance between the crack surface and all the points queried serves as a thresholding value to discern between a failing slip direction (FSD) and a non-failing slip direction (NFSD). Pseudo codes of the proposed slip direction based procedure and the standard procedure to determine the FCGR are available in Appendix A.

2.2.3.2 Micromechanical fields mining procedure

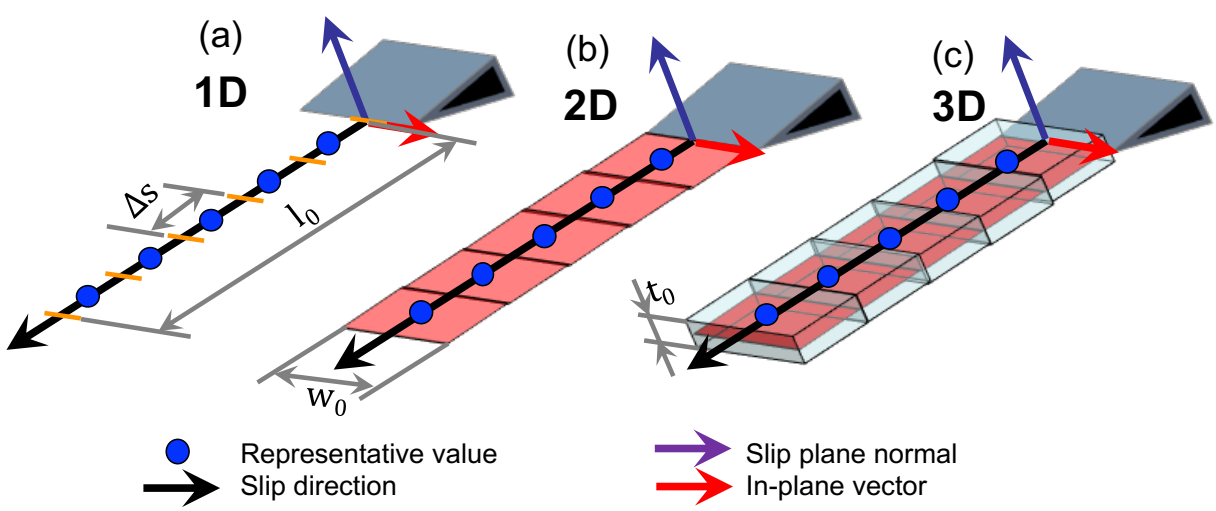

Figure 2. Schematic representation of the non-local data mining procedures, highlighting representative values and their associated regularization volume.

Similarly to the FCGR reconstruction, the micromechanical fields are collected starting from the crack front while following the available slip directions (Figure 2). Data is collected along a distance l_0 with spatial resolution (e.g. step size) Δs. However, quantities such as the accumulated plastic strain and the resolved shear stress are slip system dependent. Therefore,

while following one slip direction, data is collected for all the slip systems embedded within. Throughout this paper, this procedure will be called the 1D data-mining procedure (1D-DMP).

Moreover, when probing results of a simulation in the proximity of a singularity (i.e. the crack front), a regularization scheme should be adopted to mitigate the effect of possible spurious solutions due to unavoidable numerical instabilities. Two different regularization schemes are proposed: (i) 2D-DMP and (ii) 3D-DMP. Each regularization procedure is an augmentation of the previous. The 2D-DMP collects data on a plane accordingly oriented with respect to each slip system (Figure 2 (b)), and the 3D-DMP collects data in a plate with finite thickness (Figure 2 (c)). For all the DMPs, data is collected on an equispaced, regular grid. Parameters utilized for the above procedures are the following: (i) width of plane $w_0 = 2.8\ \mu m$, (ii) thickness of the plate $t_0 = 1.4\ \mu m$, and (iii) the step utilized to construct the equispaced, regular grid is $\Delta s = 0.35\ \mu m$.

As previously mentioned, one of the aims of this article is to evaluate the spatial correlations between the proposed non-local driving force and experimental observations. Therefore, the collected data is segmented every $0.7\ \mu m$ while moving away from the crack front, and an average value is computed for each segment. The values resulting from the averaging process are called representative values. As a note, the representative value at the crack front is not utilized as an input to build the small crack propagation framework, because its value may be influenced by the singularity imposed by the presence of the crack.

2.2.3.3 Non-Local Crack Growth Driving Force

Constructing a driving force able to capture the FCGR propagating in a BCC alloy, in which non-Schmid effects can be significant (Weinberger et al., 2013), is not the purpose of this work. Nevertheless, given the objectives of this study, the postulated driving force needs to satisfy the following requirements: (i) capture the propensity of BCC metals to deform in pencil-glide mode and (ii) account for the spatial variation of the micromechanical fields (e.g. it must use more than one local value to account for the spatial gradients). Furthermore, in a previous work, Rovinelli et al. (2017) showed that locally computed FIPs exhibit the same predictive capabilities, therefore we selected the FIP representing the maximum dissipated energy as a base for the proposed non-local driving force.

$$DF^d(s) = \sum_{\alpha=1}^{N} |\tau^\alpha(s)\Gamma^\alpha(s)| \ \forall \alpha \in d \qquad \textit{Equation 6}$$

Where d represents a slip direction and s is the index denoting the representative value while moving away from the crack front. Equation 6 is a nonlocal driving force representing the profile of the total dissipated energy along a slip direction, which will be denoted as DF for the remainder of the article.

2.3 Crack Propagation Framework

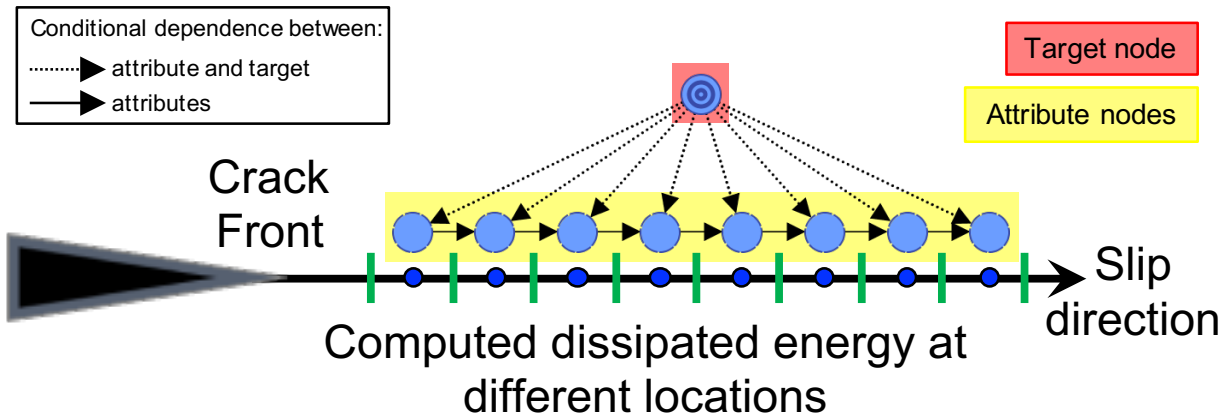

Figure 3. Schematic representation of the two augmented Naïve Bayesian networks overalid to the data mining path. Each attribute node corresponds to a representative value.

In this work, the SC problem has been separated into two different tasks: (i) identify the crack propagation direction and (ii) identify its associated FCGR. The binary variable FnF^d represents the crack propagating along a given slip direction. The continuous variable GR^d represents the FCGR of a FSD. Two distinct Bayesian networks have been implemented. The first Bayesian network, hereafter referred to as BN^{FnF}, evaluates the posterior probability of failure given the values of the DF. The second Bayesian network, hereafter referred to as BN^{GR}, evaluates the posterior probability of observing a certain FCGR given the values of the DF. Equation 7 and Equation 8 are the mathematical representations of the propositions stated above, in which the superscript d and the dependence from s have been dropped to simplify the notation. These simplifications shall hold for the rest of the article.

$$P(FnF|DF) = \frac{P(DF|FnF)P(FnF)}{\int P(DF|FnF)P(DF)dFnF} \qquad \textit{Equation 7}$$

$$P(GR|DF) = \frac{P(DF|GR)P(GR)}{\int P(DF|GR)P(DF)dGR} \qquad \textit{Equation 8}$$

In Bayesian network formalism, nodes embody variables and edges represent their conditional dependence. In classification problems, a target variable is the quantity that we want to predict, while an independent variable is called an attribute. FnF and GR are the target nodes, while the computed DF is represented by a distinct attribute for each spatial location (Figure 3). Variable discretization is performed utilizing a genetic algorithm available in Bayesialab, for which the only required parameter is the number of intervals. Furthermore, FnF is a binary variable, while GR and each $DF(s)$ have been discretized into five and seven intervals, respectively (see Appendix B for discretization edges).

The network structure selected to perform the classification is the so-called tree augmented Naïve Bayes (Friedman et al., 1997). This structure allows for conditional

dependence between different attributes. This property is critical in spatially dependent physical phenomena, such as fatigue crack growth, where the downstream value of a micromechanical field or driving force (e.g. $DF(s+1)$) is inherently related to its upstream value (e.g. $DF(s)$), and vice versa. An example of this behavior is the dislocation mechanics at the crack tip, which is influenced by the elastic stress field imposed by dislocations located at a certain distance from the crack tip (Devincre and Roberts, 1996). Figure 3 depicts the structure of BN^{FnF} and BN^{GR} overlaid with a schematic depicting the location of representative values. Each representative value corresponds to one node of the Bayesian network.

Once the model is chosen and data has been collected the parameters of the Bayesian network can be estimated from the data. The sets of data utilized to train the BN^{FnF} and BN^{GR} are selected as follow:

- BN^{FnF}: the same number of FSD and NFSD are selected to obtain a uniform prior distribution for the FnF.
- BN^{GR}: all FCGR data are utilized. A stratification procedure is utilized obtain a uniform prior distribution for the GR.

Additionally, to avoid spatial bias stationary crack front locations are randomly sampled only once. The independence of the Bayesian networks parameters from the data has been examined performing a K-fold cross-validation (see Rovinelli et al., 2017 for more details). For both Bayesian network $K = 3$ has been utilized.

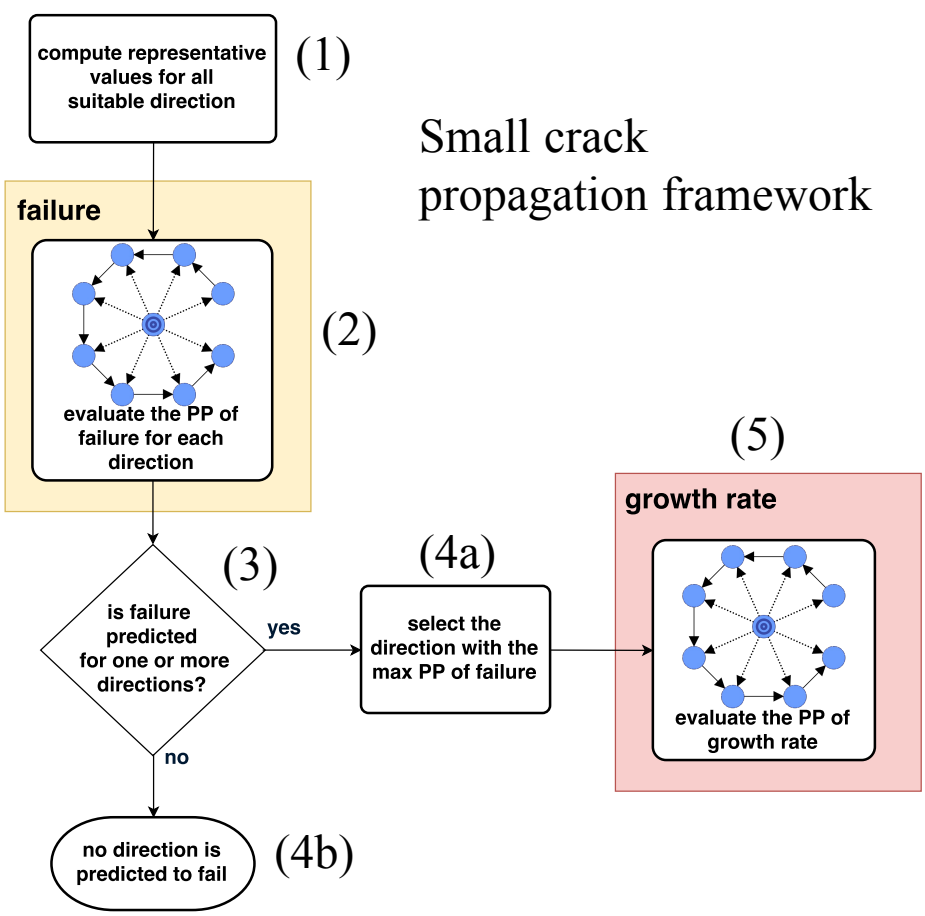

Figure 4. A workflow showing the deterministic procedure adopted to establish the FSD and its associated FCGR.

The Bayesian networks presented above have been constructed assuming that failure and propagation rate are material dependent parameters. However, at each crack front location, failure will occur only on one of the available directions. Therefore, a determinist procedure evaluating the FSD is required to resolve ambiguities (i.e. more than one slip direction may have a posterior probability of failure greater than 50%). Figure 4 is a flowchart describing the adopted deterministic procedure: (1) compute the representative values of the proposed driving force for each slip direction at a specific location, (2) compute the posterior probability of failure of each slip direction via BN^{FnF}, (3) evaluate if any slip direction exhibits failure (e.g. $P(FnF|DF) > 50\%$), (4) select the slip direction exhibiting the highest probability of failure, and (5) compute the associate FCGR via BN^{GR}.

2.3.1 Correlation quantification

In statistics, Pearson correlation coefficient (Pearson, 1895) is the standard correlation measure. However, its major limitation is the assumption of linearity embedded in its formulation. In information theory, mutual information (Shannon and Weaver, 1949) is commonly utilized to quantify the amount of information shared between two random variables (i.e. X and Y). For discrete distributions, mutual information is defined as follow:

$$MI(X,Y) = \sum_{x \in X} \sum_{y \in Y} p(x,y) log_2 \frac{p(x,y)}{p(x)p(y)} \qquad \text{Equation 9}$$

Where, x and y are indices specifying the states of X and Y, respectively, $p(x)$ and $p(y)$ are the marginal probabilities of X and Y, and $p(x,y)$ represents their joint distribution. The mutual information is a measure of uncertainty reduction on the state of X while observing the state of Y and vice versa.

Compared to the Pearson correlation coefficient, MI correctly captures nonlinear relationships, is more resilient to the presence of outliers (Correa and Lindstrom, 2013), but is not bounded between 0 and 1. Hence, to fairly compare correlations MI is normalized by the entropy (H) of the target variable (e.g. X)

$$NMI(X,Y) = \frac{MI(X,Y)}{H(X)} \qquad \text{Equation 10}$$

Where NMI is the normalized mutual information and $H(X) = -\sum_{x \in X} p(x) log_2\big(p(x)\big)$. The entropy may be considered the equivalent of the standard deviation in information theory (Correa and Lindstrom, 2013). As an interpretation, NMI can be understood as the variation of the posterior probability of X, while observing the state of Y. For example, assuming a prior probability of failure $P(FnF) = 50\%$ and a $NMI(FnF, DF) = 15\%$, means that knowing the value of the DF will imply a posterior probability $P(FnF|DF) = 35\%$ or $P(FnF|DF) = 65\%$.

2.3.2 Model performance

The performance of a classification model to predict a certain state, i, can be measured by defining two quantities: (i) reliability (Equation 11), which is the trustworthiness of the

model's prediction and (ii) precision (Equation 12) which is the ability of the model to replicate experimental observations.

$$Reliability_i = \frac{\#predictions_i^{correct}}{\#predictions_i} \quad \text{Equation 11}$$

$$Precision_i = \frac{\#predictions_i^{correct}}{\#observation_i} \quad \text{Equation 12}$$

For a classification model with N possible outcomes, its overall performance can be quantified by defining the overall reliability and precision, Equations 13 and 14, respectively.

$$Reliability_{overall} = \sum_{i=1}^{N} w_i Reliability_i \quad \text{Equation 13}$$

$$Precision_{overall} = \sum_{i=1}^{N} w_i Precision_i \quad \text{Equation 14}$$

Where w_i is a weighting factor defined as $w_i = \#observation_i / \#observations_{total}$. In this work $N = 2$ for BN^{FnF} and $N = 5$ for BN^{GR}, respectively. The above quantities (Equations 13 and 14) are used in this work to evaluate the overall performance of BN^{FnF} and BN^{GR}. A model exhibiting high reliability and precision can be considered trustable.

2.4 Small crack – grain boundary interaction

When the crack front impinges upon a GB, its path cannot be predicted utilizing the proposed non-local driving force because it does not account for microplasticity in the adjacent grain. Additionally, crystal plasticity do not capture the physics of slip transmission at GBs because the residual Burgers vector is not conserved (Acharya, 2007; Acharya et al., 2008; Mach et al., 2010). Therefore, several criteria have been either selected from the literature or postulated (Table 2) and used to predict in which slip system the crack will propagate after crossing a GB.

The pencil-glide model has been adopted to capture the predominant deformation mechanism of the analyzed BCC alloy. Nevertheless, a SC propagates by incrementing its area. Therefore, slip transmission criteria based upon slip planes have also been included in the analysis.

Table 2. Formulation and description of the investigated slip transmission criteria. Figure 5 is a schematic defining the geometric variables required to compute the slip transmission criteria.

Equation		Description
$\max_p\left(cos(\theta^p)\right)$	Equation 15	Minimum twist angle (Zhai et al., 2000)
$\max_p\left(cos(\psi^p)\right)$	Equation 16	Minimum tilt angle

$\max_{d}\left(cos(\kappa^{d})\right)$	*Equation 17*	Minimum misalignment between incoming and outgoing slip directions (Gibson and Forwood, 2002)
$\max_{p}\left(\left[\left(\boldsymbol{n}_c \cdot \boldsymbol{n}_o^p\right)\left(\boldsymbol{b}_c \cdot \boldsymbol{b}_o^p\right) + \left(\boldsymbol{n}_c \cdot \boldsymbol{b}_o^p\right)\left(\boldsymbol{b}_c \cdot \boldsymbol{n}_o^p\right)\right]\right)$	*Equation 18*	Maximization of slip system alignment (Livingston and Chalmers, 1957)
$\max_{p}\left(cos(\kappa^{p})cos(\psi^{p})\right)$	*Equation 19*	Minimization of the product of the misalignment of slip direction and tilt angle (Luster and Morris, 1995)
$\max_{p,d}\left(cos(\kappa^{p})cos(\theta^{p})\right) \quad \forall d \in p$	*Equation 20*	Minimization of the product of the misalignment between slip direction and twist angle (Shen et al., 1986)
$\min_{d}(\lVert \boldsymbol{b}_o^d - \boldsymbol{b}_c \rVert)$	*Equation 21*	Minimization of the residual Burgers vector (Lee et al., 1989)

Where θ, ψ represent the twist and tilt angles between the crack plane and the available slip planes in the adjacent grain, κ is the angle of misalignment between the slip direction embedded in the crack plane and the one available in the neighboring grain. Symbols $\boldsymbol{n}$ and $\boldsymbol{b}$ represent the slip plane's normal and the Burgers vector, while superscripts p and d are indices referring to the available slip plane and slip direction, respectively. Additionally, subscripts c and o represent the crack and the outgoing slip planes. Figure 5 is a schematic representation of the geometrical meaning of the aforementioned quantities.

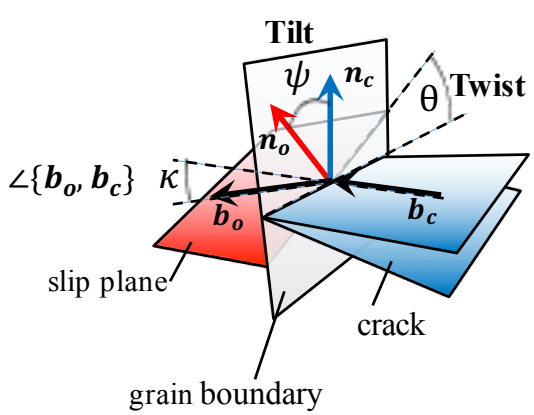

Figure 5. Schematic depicting the crack (blue) impinging upon a grain boundary (light gray) and one of the slip plane (red) available in the adjacent grain. All the geometrical quantities characterizing the interaction of the crack with the neighboring slip systems are illustrated.

To accurately compute the tilt and twist angle along the line of intersection between the crack surface and the GB plane, the normal of the GB plane have been computed by utilizing diffraction contrast tomography results and applying the method proposed by Lieberman et al. (2015). The suggested scaling, equivalent weight method has been utilized in the calculations, with a sphere radius $r = \sqrt{3}\ voxel$. Once the normal is known, θ and ψ can be computed be means of the following equations:

$$\theta = acos([\boldsymbol{n}_c \times \boldsymbol{n}_{GB}] \cdot [\boldsymbol{n}_o \times \boldsymbol{n}_{GB}])$$ *Equation 22*

$$\boldsymbol{v} = [\boldsymbol{n}_{GB}, -\theta]$$ *Equation 23*

$$\psi = acos(\boldsymbol{n}_c \cdot [\boldsymbol{v} * \boldsymbol{n}_o])$$ *Equation 24*

where $\boldsymbol{n}_{GB}$ is the normal of a GB, $\boldsymbol{v}$ is the axis-angle representation of the rotation required to remove the twist angle, and symbol $*$ implies rotating the second argument accordingly to $\boldsymbol{v}$ (e.g. using Rodrigues rotation formula).

3 Result and discussion

3.1 Slip direction based modeling

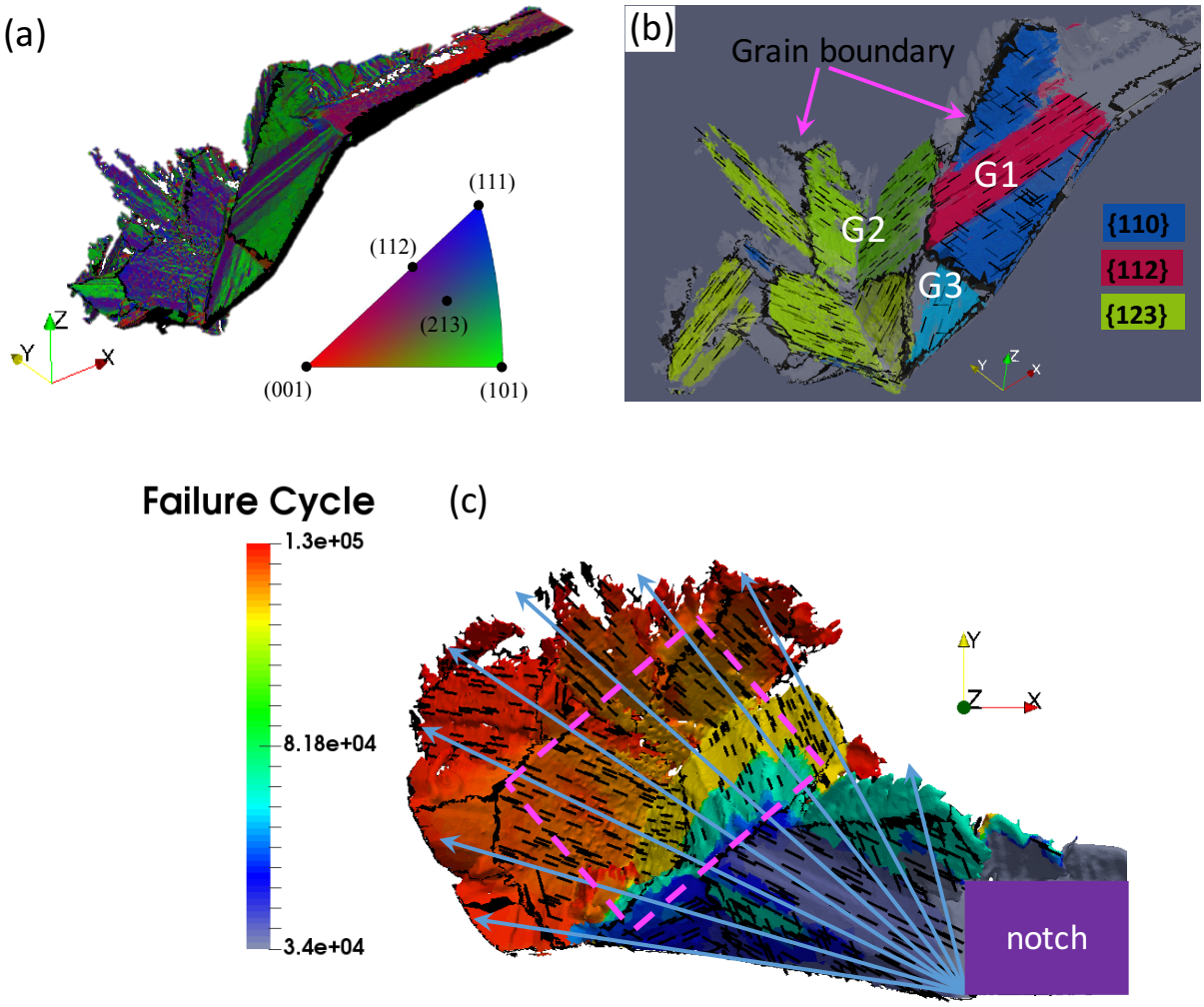

Figure 6. The crack surface is colored accordingly to the: (a) crystallographic orientation of each facet; (b) plane of failure identified by the macro feature tracking algorithm; (c) cycle of failure. Black, tortuous lines always represent grain boundaries. Short straight lines represent slip direction embedded in the plane of failure (b and c). In (c): (i) blue arrows represent the FCGR for elliptic propagation, and (ii) the magenta box highlights the location where abrupt changes of the propagation direction can be observed.

3DXTSM results are coarsened utilizing a smoothing procedure to remove small features of the crack surface that cannot be modeled via the current simulation setup. The effect of the smoothing method (see Appendix C for a pseudo-code algorithm) is to coarsen the scale of the analysis to allow removal of high-frequency features while preserving long-range attributes.

Figure 6 (a) depicts the final crack surface, in which each of its facets is colored accordingly to its local orientation. The first noticeable feature is that only few regions are assigned to the {110} planes (i.e. green), while most of the surface is assigned to slip planes belonging to {112} or {123} families (i.e. purple). Herbig et al. (2011) conjectured that the reason behind the observed plane of failure distribution might be related to the resolution

utilized when performing 3DXTSM. In fact, at the atomic scale each {112} plane can be decomposed into two alternating {110} planes, and each {123} plane can be decomposed in three {110} planes. Figure 6 (b) depicts the crack surface colored accordingly to the slip plane identified by the smoothing procedure. Even at a coarser scale the crack propagates exploiting all slip plane families. This observation not only reinforces the need to include all sets of slip planes when simulating BCC materials (Rovinelli et al., 2017b; Weinberger et al., 2013), but shows that small crack propagation is a multiscale phenomenon.

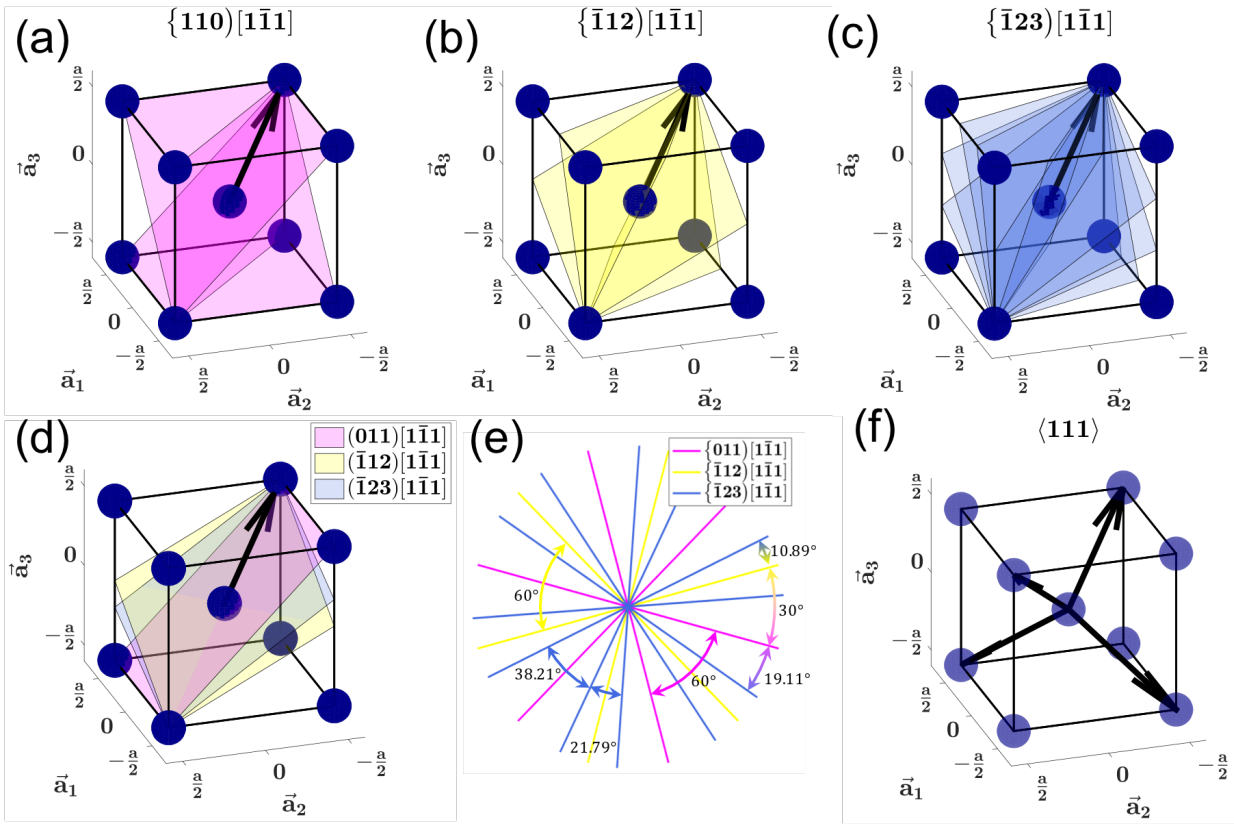

Figure 7. Schematics depicting a single unit cell of a BCC crystal. Blue spheres represent atoms, arrows slip direction, and colored surfaces and lines slip planes. Subfigures (a-c) depict the $\{011\}[1\bar{1}1]$, $\{\bar{1}12\}[1\bar{1}1]$, and $\{\bar{1}23\}[1\bar{1}1]$ slip systems, respectively. (d) A geometrical representation of a slip direction and several slip planes revolving around it. (e) A schematic representing the distance (in degree) between all the slip planes embedded into a single slip direction. (f) A unit cell of a BCC crystal highlighting the four independent slip directions.

The short straight black lines depicted in Figure 6 (b) represents slip directions embedded into the assigned plane of failure. BCC metals have 48 slip systems, which are divided into three families and partitioned as follow:

- 12 - $\{011\}\langle 11\bar{1}\rangle$
- 12 - $\{112\}\langle 11\bar{1}\rangle$
- 24 - $\{123\}\langle 11\bar{1}\rangle$

Counting the number of independent slip plane, it can be found that there are 6 unique $\{110\}$, 12 unique $\{112\}$, and 24 unique $\{123\}$ slip planes, for a total of 42. On the other hand, only four independents $\langle 11\bar{1}\rangle$ slip directions exist (see Figure 7 (f)). Therefore, many slip systems must share the same slip direction. Figure 7 (a-c) are schematics representing the set of 3 $\{011)[1\bar{1}1]$, 3 $\{\bar{1}12)[1\bar{1}1]$, and 6 $\{\bar{1}23)[1\bar{1}1]$ slip systems, for a total of 12. Plotting all the slip planes associated with a specific slip direction in a single unit cell unveils their spatial arrangement (Figure 7 (d,e)).

Taylor and Elam showed that the plastic deformation mechanism in BCC metals is quite different from the one observed in FCC materials (Taylor and Elam, 1926). This difference can be related to the crystalline structure and the inherited dislocation dynamics. In fact, FCC crystals possess only four close-packed slip planes, in which only two share the same slip direction. In contrast, BCC crystals have twelve different slip planes embedding the same slip direction. Dislocations are allowed to cross-slip (i.e. change slip plane) only if their Burgers vector (i.e. the slip direction) is preserved (Hull and Bacon, 2011). Hence for a dislocation gliding on a slip plane in a FCC material there is only one option for cross-slip at an angle of $109.47°$, while in a BCC material there are eleven candidates. Moreover, considering the nearest neighbors, in BCC crystals the maximum cross-slip angle is $19.10°$, while the minimum is $10.89°$ (see Figure 7 (e)). Given such slip plane arrangements, it is likely that more than one slip plane is subject to similar micromechanical fields, thus making a slip plane analysis almost useless. Hence, in this work, the slip direction based modeling approach is adopted. This approach not only is consistent with pencil-glide deformation mechanism, but also reduces the number of degrees of freedom required to predict the crack propagation direction from 48 (e.g. the number of slip systems) to 4 (e.g. number of slip directions).

Figure 6 (c) depicts the crack surface colored by the failure cycle number. Moreover, the black short lines represent the slip direction associated with the slip planes identified by the smoothing algorithm. The blue vectors represent the imposed propagation path assuming a corner crack with a unique center. The transition between each crack step (e.g. color) is strikingly better reproduced by following the slip directions (i.e. short straight lines) rather than assuming the propagation event originates from a unique crack center (i.e. blue vectors). This correlation is not only evident close to the notch, but is also visible in later stages on the region highlighted by the dashed magenta rectangle (Figure 6 (c)). We hypothesize that the reason for the agreement between the crack propagation direction and the slip directions is linked to the propensity of BCC materials to deform accordingly to the pencil-glide model.

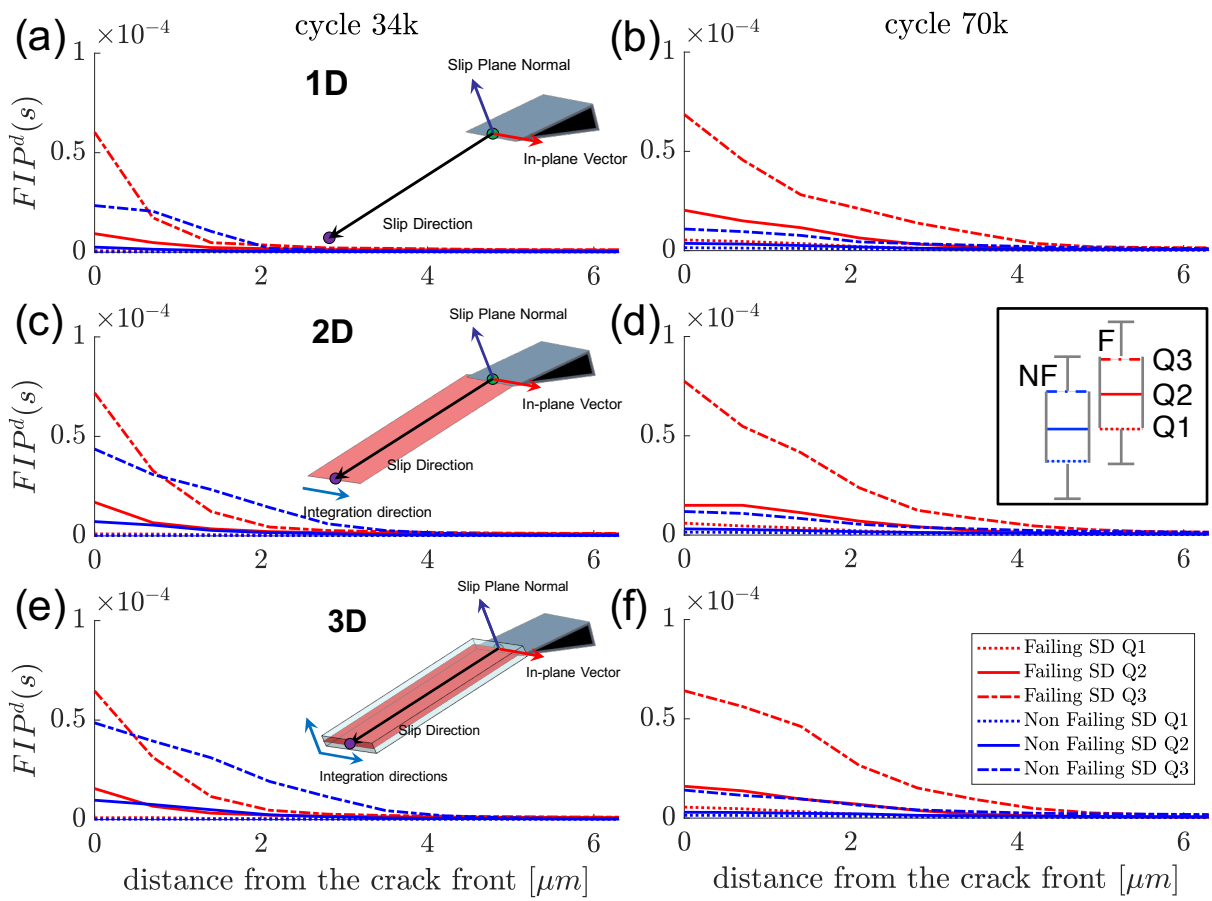

Figure 8. Comparison of the computed DF (Equation 6) applying the three proposed data-mining procedures. Figure 8 is organized as a table. The columns, subfigures (a,c,e) and (b,d,f), depict results for cycle 34k and 70k, repsectivley. The rows, subfigures (a,b), (c,d), and (e,f), correspond to results obtained by appling the 1D, 2D, and 3D-DMP, respectively. Red lines represent FSD, and blue lines repsents NFSD. Moreveor, different line styles represent different quartiles: (i) dotted lines represent the first quartile (i.e. Q1), (ii) continuous lines represent the second quartile (i.e. Q2), and (iii) dashed-dotted lines represent the third quartile (Q3). Mathematically, Q1, Q2, and Q3 represent values of a distributed variable where its cumulative distribution function corresponds to $25\%, 50\%$, and 75%, respectively.

Figure 8 depicts values of the DF (Equation 6) computed by applying the three proposed DMPs for two different crack snapshots (i.e. cycle 34k and 70k). Moreover, to gain some insight on the ability of DF to statistically capture the SC path data is partitioned between the FSD (i.e. red lines) and NFSD (i.e. blue lines), and a quartile analysis is performed (see Figure 8 caption for details). As a note, $Q1$, $Q2$, and $Q3$ (i.e. quartiles) are values at which the cumulative distribution function corresponds to $25\%, 50\%$, and 75%, respectively.

Focusing on one crack snapshot at a time (e.g. cycle 34k, Figure 8 (a,c,e)) and comparing results of the three proposed data mining procedures with each other (e.g. comparing Figure 8 (a) with Figure 8 (c)) only minor differences in the location of each quartile can be observed. Noticeable variations are confined between the crack tip and a distance smaller than 2 μm. It has already been mentioned that results at the crack tip will be discarded to avoid the influence of numerical instabilities. However, some discussion is required to explain the observed variations.

Comparing the location of the third quartile of the FSD (i.e. red, dashed-dotted line) of the 1D-DMP and 2D-DMP (i.e. comparing Figure 8 (a) with Figure 8 (c)), the latter exhibits higher values. The opposite is true comparing results of the 2D-DMP with the ones of the 3D-DMP (e.g. comparing Figure 8 (c) with Figure 8 (e)). The 2D-DMP mitigates local perturbation in the micromechanical fields associated to the tortuous nature of the crack front better than the 1D-DMP. Moreover, results obtained via the 3D-DMP may underestimate the upper bound, due to excessive averaging outside the region of interest (i.e. the plastic zone), which is limited in size for high cycle fatigue regimes.

The small influence of the regularization region on the distribution of FIPs has been reported by Castelluccio and McDowell (2015), suggesting that bands (i.e. thick plates) should be preferred to predict crack nucleation in FCC metals. However, in this work, the focus of the analysis is SC propagation and not nucleation. Since a SC propagates by increasing its area and dislocation motion is predominantly a planar phenomenon in this alloy, the 2D-DMP procedure has been selected.

As mentioned earlier, the ability of the proposed driving force to discern between the FSD and NFSD can be elucidate through statistical analysis. If the quartiles (i.e. Q1, Q2, and Q3) of two different distributions overlap, it follows that the two distributions are similar. Focusing on Figure 8 (c), it can be noticed that lines representing the first and second quartile (i.e. Q1 and Q2) of the FSD and NFSD almost overlap along the examined length. Examining the third quartile (i.e. Q3), data shows that the FSD exhibit a higher value at the crack tip compared to NFSD, but this trend is reversed while moving away from the crack tip. Therefore, no clear conclusion can be drawn from this case. A different trend is observed investigating results of cycle 70k (Figure 8 (d)), where the two distributions are almost offset by one quartile (see inset in Figure 8 (d) for a schematic representation). In this scenario, Q1 of the FSD almost overlap with Q2 of the NFSD, and Q2 of the FSD is higher than Q3 of the NFSD, thus there is a significant distance between values computed for the FSD and NFSD.

From a micromechanical perspective, the above analysis entails that when the crack starts to propagate (e.g. cycle 34k) the micromechanical fields of FSD and NFSD do not show a strong statistical difference. At cycle 34k, the crack is so minute (see Figure 6 (c)) that the imposed stress-field is insufficient to generate enough plasticity to clearly distinguish between the FSD and NFSD. This effect may also be amplified by the CP-FFT formulation, where the crack cannot be considered perfectly sharp. Conversely, at cycle 70k, the crack has propagated to a substantial length, thus imposing a stronger stress field. The latter results in more distinct distributions of FSD and NFSD. The above entails that the DF can statistically capture the difference between a FSD and a NFSD, therefore further sustaining the slip direction based modeling for SC propagation in BCC metals. Moreover, considering that cycle 70k represents the longest crack analyzed in this work and the results of all the proposed procedures exhibit saturation before $6\ \mu m$ (see Figure 8 (b,d,f)), $l_0 = 6.3\ \mu m$ has been selected.

3.2 Probabilistic small crack propagation framework

Table 3. Overall performance of the trained Bayesian network. Specifically: (a) and (b) shows overall reliability and precision of BN^{FnF} and of BN^{GR}, respectively; (c) represents the distribution of the predictions obtained via BN^{GR}.

(a) Fail Non Fail

Overall Reliability	**78%**
Overall Precision	**77%**

(b) Growth Rate

Overall Precision	**64%**
Overall Reliability	**64%**

(c) Growth Rate Training Predictions

	Underestimated	**16%**
PDF	**Correct**	**64%**
	Overestimated	**20%**

As described earlier, Bayesian networks are utilized to establish the posterior probability of failure of a slip direction and its associated FCGR in a non-local fashion, by imposing computed values of the DF. Table 3 (a) and (b) depicts performance of BN^{FnF} and BN^{GR}, respectively. The overall reliability and precision of BN^{FnF} are close to 80%, while the ones of BN^{GR} are close to 64%. Therefore, BN^{FnF} can be considered reliable and capable of accurately replicating the experimental observations, while results of BN^{GR} need to be further discussed. First, it should be mentioned that BN^{FnF} is a binary classifier (i.e. a slip direction can be classified only as a FSD or NFSD), while BN^{GR} is a multi-label classifier (i.e. the FCGR is a continuous variable discretized into five intervals). Furthermore, the crack surface encompasses only few grains, and data representing the FCGR is limited to a few hundred points, hence the data set utilized to train BN^{GR} may not be rich enough to capture the overall FCGR behavior. Table 3 (c) shows the distribution of prediction obtained with BN^{GR} with respect to the experimental data, which is computed by averaging the confusion matrix (i.e. the matrix comparing the number experimental observations and prediction results for each bin). As noted, the framework generates an almost symmetrical distribution of under and over-estimated FCGR (i.e. 16% and 20%, respectively). The symmetric distribution of incorrect predictions shows that BN^{GR} parameters are not over-fit and strengthen the hypothesis that not enough data is present to accurately capture the overall FCGR behavior and it is comparable with experimental measurements errors given the size of the crack and utilized spatial resolution. Moreover, the proposed DF shows much better prediction quality than locally computed FIPs ($reliability \approx 37\%$, $precision \approx 31\%$, Rovinelli et al., 2017).

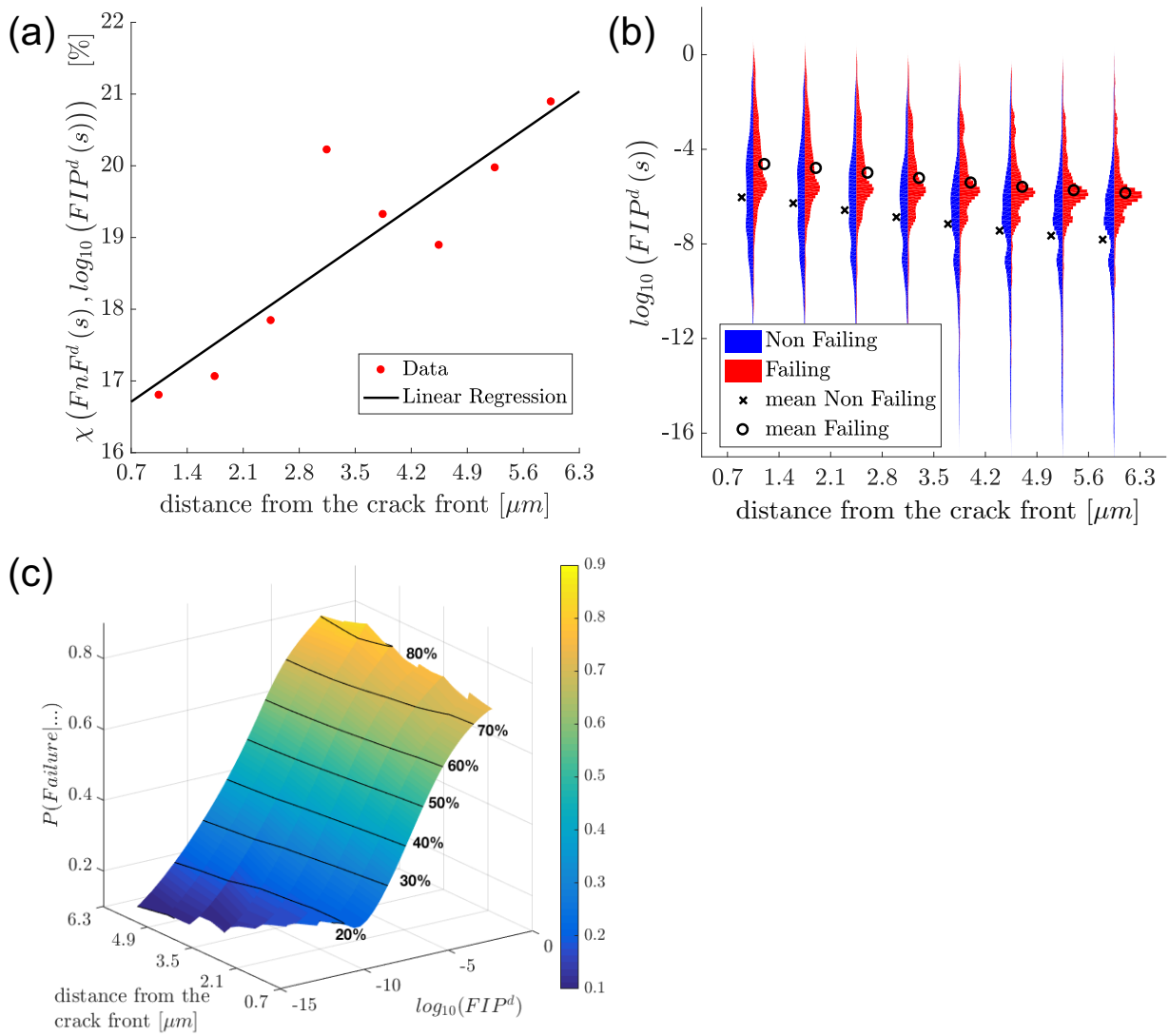

Figure 9: (a) Spatial correlation between the proposed non-local small crack driving force and the distance from the crack front and the associated regression line. (b) Violin plots comparing normalized distributions of the computed driving force values as a function of the distance from the crack front; symbols "∘" and "×" represent mean value of the FSD and NFSD, respectively. (c) Posterior probability of failure given: the distance from the crack front and the value of the DF.

The strength of the correlations embedded in the Bayesian networks probability tables can be quantified utilizing NMI (Equation 10). Specifically, the correlation between the probability of failure, and the dissipated energy is computed as follows:

$$\chi(s) = NMI\big(FnF, \log_{10}\big(DF(s)\big)\big) \qquad \textit{Equation 25}$$

Hence, a correlation value is obtained for each spatial location s (i.e. for each attribute node of BN^{FnF}). Figure 9 (a) depicts the spatial relationship between χ and the distance from the crack front and, as mentioned in Section 2.3.1, the value of χ represents the reduction in uncertainty on the probability of the crack to propagate along a given slip direction. The correlation increases almost monotonically moving away from the crack tip, noting that: (i) this trend will not continue indefinitely, (ii) the variation in magnitude of χ is limited, and (iii) the

correlation has been computed in logarithmic space to capture the influence of micro-plasticity away from the crack tip.

To unveil the reason beneath the observed unexpected trend, raw distributions of the proposed driving force need to be investigated in more detail. Figure 9 (b) depicts normalized distributions of the computed DF for the different representative values. Moreover, all the data belonging to the training dataset of BN^{FnF} has been used. Distributions are graphed separately for the FSD (i.e. red) and NFSD (i.e. blue). Symbols denote mean values of the graphed distributions.

Mean values confirms the trend observed in Figure 8 (d). Focusing on distributions shape and range, the following tendencies are detected: (i) distributions representing NFSDs do not show localized high-density regions and exhibits long tails towards low values, and (ii) distributions depicting FSDs are almost normal, exhibits pronounced tails towards high values, and the probability of their modal value (i.e. the most frequent) increases with distance. Moreover, while moving away from the crack tip the range of shared values between the FSD and NFSD diminish.

Thus, it becomes apparent why better correlations are observed away from the crack tip. For instance, close to the crack tip (e.g. $0.7 < s < 1.4\ \mu m$) the distributions representing the FSD and NFSD share a broad range of values and exhibits almost comparable densities. Therefore, observing a value of the DF belonging to their shared region does not provide useful evidence to discern between a FSD and NFSD, therefore lowering the correlation. Far away from the crack tip (e.g. $5.6 < s < 6.3\ \mu m$), distributions are more distinct than in the previous case. At this location, the range of shared values of the FSD and NFSD is smaller, and their probability densities are dissimilar. Therefore, observing a computed driving force value in the shared region will provide more information to evaluate the posterior probability of failure.

To quantify the effect that the DF has on the posterior probability of failure, we utilized the Bayesian network framework to systematically change the mean of each attribute node and compute the associated posterior probability. The results of the above procedure are presented in Figure 9 (c), which is a surface representing the posterior probability of failure as a function of the DF and distance from the crack front. It should be noted that this surface can be used only for the first observation, because once evidence has been imposed, the joint probability changes, thus altering the effect of the next observation.

The surface in Figure 9 (c) exhibits a sigmoidal shape and it can be associated to a multidimensional logistic regression. Therefore, the contour line representing 50% probability can be interpreted as the threshold value for failure, while the range of the DF between low and high probability (e.g. between 30% and 70%) are indicative of the overall uncertainty. Moreover, values of the DF are proportional in logarithmic space to the posterior probability of failure, supporting the previous discussion and being in accordance with the premise that the amount of plasticity, or any of its associated quantities, is directly correlated to the probability of failure. Furthermore, the range of the posterior probability slightly increases moving away from the crack front accordingly to the trend exhibited by the correlations in Figure 9 (a).

The above results can also be explained from a micromechanical perspective. In the proximity of the crack tip, the imposed stress field is so intense that multiple dislocations with distinct Burgers vectors (George and Michot, 1993) are emitted. In BCC materials, the abundance of slip planes aids the above process and explains comparable densities of the DF

distributions for a FSD and NFSD in proximity of the crack front (see Figure 9 (b), $0.7 < s < 1.4\ \mu m$). Away from the crack tip, the stress field imposed by the presence of the crack decays proportionally to $1/s$, reducing the number of slip systems favorably oriented for dislocations glide. Far away from the crack tip, a FSD is much more likely to show a high value of the DF than a NFSD (Figure 9 (b), $5.6 < s < 6.3\ \mu m$), suggesting that slip directions embedded in larger plastic zones are the preferred direction for failure. Therefore, supporting the proposition that SC propagation is a non-local phenomenon driven by micro-plasticity at the edges of the plastic zone (Devincre and Roberts, 1996).

The above findings also suggest that some care should be used when utilizing a scalar quantity (such as a FIP) as the small crack driving force. The reasons are two-fold: (i) if the FIP is computed by sampling data at a specific distance from the crack front (e.g. as if only one representative values is used), then the best distance to sample values needs to be identified and (ii) if the FIP is computed by averaging along a specific region (e.g. averaging several representative values, Castelluccio et al., 2016; Musinski and McDowell, 2016) then care should be used, because the correlation is a function of the distance. A more robust strategy to compute a scalar FIP is to sample while moving away from the crack front until a predetermined threshold value of the FIP is found, and only then compute a density. This method helps to account for the plastic zone size and micro-plasticity ahead of the crack.

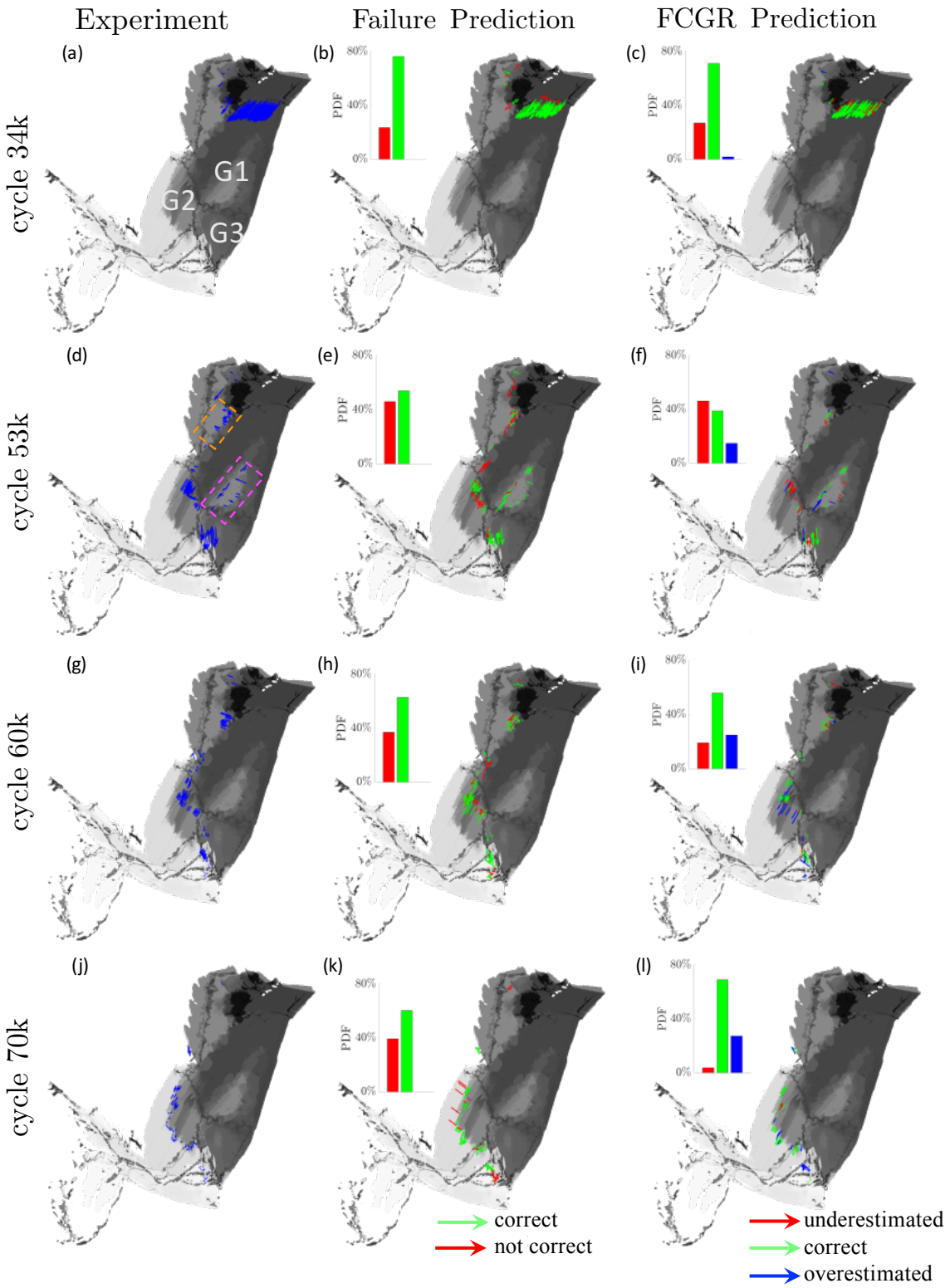

Figure 10. Results of the small crack growth propagation framework compared to experimental observations. Rows 1-4 (i.e. subfigures (a,b,c), (d,e,f), (g,h,i), and (j,k,l)) represent different crack snapshots. Columns 1-3 (i.e. subfigures (a,d,g,j), (b,e,h,k), and (c,f,i,l)) depict experimental observations, predictions of the FSD, and predictions of the FCGR, respectively. The vectors' length is proportional to the observed or computed FCGR. Histograms in Columns 2 and 3 summarize the distributions representing the amount of correctly predicted FSDs and of correctly, over, and under-estimated FCGR predictions.

Figure 10 compares results obtained by utilizing the proposed small crack propagation framework with experimental observations for different crack snapshots. All the subfigures depict the crack surface colored by cycles to failure (i.e. from black to white), in which darker regions represent grain boundaries. Vectors on the crack surface represent slip directions (see Figure 10 caption for detail) and begin at the crack front. The vectors' length is proportional to the observed or computed FCGR. At each crack front location, if the predicted FSD is the same as the experimentally observed one, then it is classified as correct (e.g. green, Figure 10 (b,e,h,k)). Moreover, for correctly predicted FSD, the computed FCGR is compared against experimental observations (Figure 10 (c,f,i,l)) and classified as correct (i.e. green), underestimated (i.e. red) or overestimated (i.e. blue). The above classification is performed by quantizing predictions accordingly to the discretized FCGR distribution (see Appendix B for bin edges). Histograms in Figure 10 (b,e,h,k) depict the distribution of correctly captured FSDs, and the ones in Figure 10 (c,f,i,l) represent the distribution of the FCGR predictions.

The analyzed crack snapshots have been selected as follows: (i) cycle 34k and 70k are the first and last analyzed propagation cycles, (ii) cycle 53k represents the crack snapshot exhibiting the worst predictions, and (iii) cycle 60k is a representative example of the mean predictive performance of the framework. The propagation of the analyzed crack proceeds as follows (see Figure 10 (a) for grain nomenclature):

1. At cycle 34k, the crack propagates from the notch on one of the available $\{112\}$ planes available in Grain 1. The observed FCGR is almost uniform.
2. At cycle 53k, the crack partially propagated into Grains 1 and 3, and it is pinned at the GB between Grains 1 and 2. The portion of the crack still embedded in Grain 1 is switching the plane of propagation from the initial $\{112\}$ to two distinct $\{110\}$ planes (orange and magenta box in Figure 10 (d)). At this stage, a big ligament of material is present in Grain 1 (see magenta box in Figure 10 (d)). Propagation in Grain 3 occurred on a $\{110\}$ plane.
3. At cycle 60k the ligament has almost failed; the crack crossed the GB between Grains 1 and 2 propagating on one of the available $\{123\}$ planes in Grain 2. In Grain 1, the crack is still propagating on a $\{110\}$ plane. Grain 3 has almost failed.
4. At cycle 70k, Grain 3 failed, the crack is propagating in Grain 2 on the $\{123\}$ plane and is almost completely intragranular.

The spatially-resolved, small crack propagation framework correctly predicts 60% of the analyzed crack front locations when establishing the propagation direction, and of the above 60%, it properly estimates the FCGR 55% of the time. However, the amount of correct predictions is dependent upon the crack front location.

In general, when the crack front is mainly intragranular (e.g. cycles 34k, 60k and 70k, Figure 10 (a,b,c), (g,h,i) and (j,k,l), respectively) the amount of correct predictions is higher compared to the overall rate, and incorrect predictions do not spatially cluster together. Conversely, when a significant portion of the crack front becomes intergranular, a significant reduction in the quality of prediction is observed. The above scenario is illustrated by cycle 53k (i.e. Figure 10 (e,f)). Specifically, a high density of incorrectly selected FSDs and overestimated FCGR can be found in the proximity of the GB between Grains 1 and 2. Nevertheless, after the

crack overcomes the GB (e.g. cycles 60k and 70k, Figure 10 (h) and (k), respectively), the framework recovers its ability to predict both the FSD and FCGR.

As mentioned, the FCGR reconstruction procedure requires a minimum available distance l_0 between the crack front and the first GB, otherwise the analyzed slip direction is not sampled. Therefore, some degradation of predictive performance is expected in the proximity of a GB. Another factor decreasing the percentage of correct predictions for the above scenario may be the limited amount of data available for it. In fact, through all the 3DXTSM results, only in a few instances, the distance between the crack front and GBs is suitable to capture the interaction between them. Therefore, it can be inferred that the proposed framework is able to statistically reproduce the behavior of a tortuous small crack propagating in a polycrystalline BCC alloy, if most of the crack front does not interact with the GBs.

3.3 Small crack – grain boundary interaction

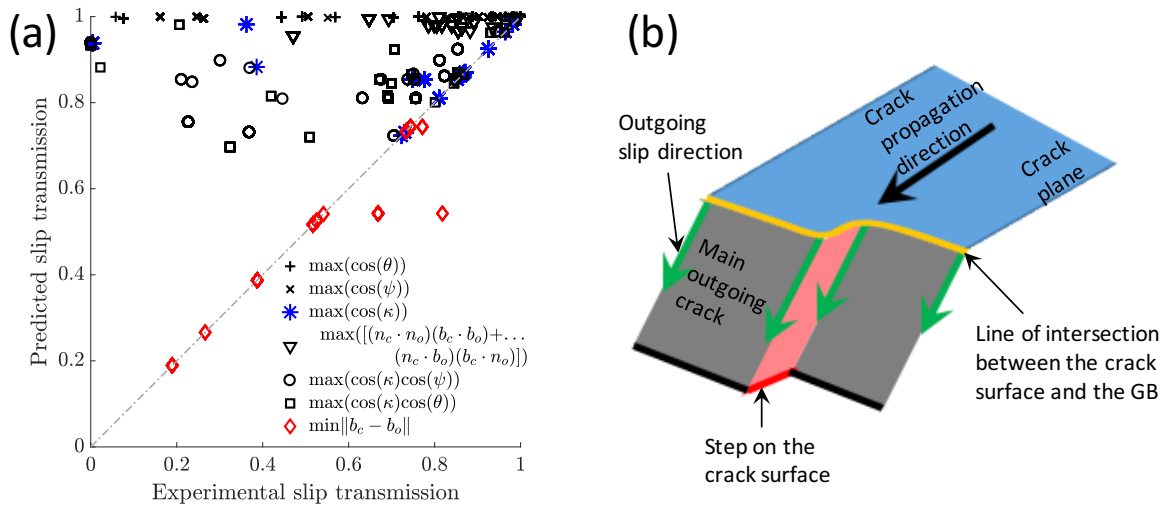

Figure 11. Correlation between the computed slip transmission criteria with respect to their experimental value. The legend shows equations of the investigated slip transmission criteria (for name, reference, and description refer to Table 2). The dashed-dotted line represents the perfect correlation. (b) Schematic representing the formations of steps on a crack surface after propagating in the adjacent grain while minimizing the residual Burger vector.

As explained, the proposed propagation framework exhibits limited predictive capabilities when a portion of the crack front impinges upon a GB. Therefore, several slip transmission criteria have been scrutinized to establish the predictive nature for the plane or direction of failure when the small crack crosses a GB. Moreover, when performing the analysis all slip plane families (i.e. $\{110\}$, $\{112\}$, and $\{123\}$) have been considered as suggested by Schäf et al. (2013).

Figure 11 (a) illustrates the results obtained by applying the selected criteria (Equations 15-21) and comparing them with experimental results. The dashed dotted line is the reference for correct predictions. Black and colored symbols represent slip planes, and slip directions based criteria, respectively.

Inspecting Figure 11 (a), it is evident that only one of the investigated slip transmission criteria exhibit a high correlation between experimental results and calculations, particularly the minimization of the Burgers vector (i.e. red diamond, Lee et al., 1989). Sangid et al. (2011) investigated slip transmission and nucleation at GBs in pure Nickel, observing that the criterion

proposed by Lee et al. (1989) provides an exact match with results of molecular dynamics simulations. Recently, Schäfer et al. (2016) experimentally investigated the resistance of the GBs to slip transmission in a Nickel-based superalloy and confirmed that the minimal Burgers vector is key to establish the active slip system in the adjacent grain. Conversely, all slip plane-based transmission criteria show poor correlations. Most of the predictions can be found in upper region of Figure 11 (a) meaning that a well aligned slip system is always present in the adjacent grain. Therefore, for BCC materials slip plane-based transmission criteria are not good candidates to predict on which slip system the SC propagates after crossing a GB.

Alternating green and purple striations visible on the crack surface within Grains 1 and 3 in Figure 6 (a) can also be explained by the minimization of the residual Burger vector. The line of intersection between a small crack and a GB plane is not straight because the crack surface is tortuous and the GB plane has a curvature. Due to the minimization of the residual Burgers vector, steps on the crack surface will appear at locations in which the line of intersection exhibits strong deflections. Once a step appears on the crack front, it persists throughout the propagation process and its wake generates a striation aligned with the crack propagation direction. Experimental results suggest that these striations are crystallographic in nature (Figure 6 (a)). Figure 11 (b) is a schematic depicting the above mechanism. Finally, we note that the minimization of the residual Burgers vector may be embedded in the proposed propagation framework to improve the predictions when the crack impinges upon a GB.

4 Conclusions

In this work, 3DXTSM results were coupled with CP-FFT simulations to investigate the behavior of a small crack propagating through a beta titanium alloy. On the premise that BCC materials deform accordingly to a pencil-glide model, 3DXTSM results have been reinterpreted accordingly.

Experimental data shows that during the early stages of crack propagation, the FCGR better aligns with slip direction rather than with the radial line starting from a single crack center. Therefore, a slip direction modeling approach has been proposed, resulting in:

- A reduction in the number of degrees of freedom required to describe the small crack propagation. From 42 slip-planes to 4 slip-directions.
- A slip direction based non-local data mining procedure, complemented by different regularization schemes.
- A non-local small crack driving force based on the dissipated energy accumulated along a slip direction.

To analyze the results of the pencil-glide modeling approach, a data driven, spatially-resolved non-local probabilistic small crack propagation framework has been developed. Results show that:

- The SC problem can be divided into two separate problems: (i) identify the direction of propagation (i.e. FSD) and (ii) estimate the propagation rate of the FSD.
- The non-local driving force statistically captures the difference between a FSD and NFSD.
- Correlations between the proposed driving force and the observed propagation behavior are spatially dependent. Specifically, a slight increase is observed moving away from crack front, confirming that for high cycle fatigue, SC propagation is a non-local phenomenon driven by micro-plasticity at the edge of the plastic zone. Based on the above, care has been advised when using a scalar driving force, and a methodology to mitigate the effect of spatially varying correlations has been proposed.
- The propagation framework exhibits consistent predictions for intragranular cracks, thus making it suitable to evaluate the path of tortuous cracks. However, a degradation in performance is observed when a considerable portion of the crack front interacts with a grain boundary.
- The predictions of the FSD are accurate 60% of the time, and the FCGR is correctly captured 55% of the times. These results are a noticeable improvement compared to Rovinelli et al. (2017), where locally computed FIPs show an average reliability between 33% and 41%.

Moreover, to elucidate the interaction between a SC and a GB, several slip transmission criteria have been selected and applied to 3DXTSM results. The analysis shows that in BCC materials a SC impinging upon a GB propagates in the adjacent grain accordingly to the slip direction minimizing the residual Burgers vector. The minimization of the residual Burgers vector

together with the non-straight line of intersection between a SC and GB also explains the formation of striations of the crack surface in adjacent grain parallel to the direction of crack propagation.

5 Acknowledgements

M. D. Sangid and A. Rovinelli gratefully acknowledge support from the Air Force Office of Scientific Research under Contract No. FA9550-14-1-0284.

6 Appendix

A: Direction based fatigue crack growth rate reconstruction algorithm

A.1 Standard procedure

The standard procedure to reconstruct the crack growth rate is the following:

1. Squeeze the 3D crack front on the plane perpendicular to the loading axis (i.e. the crack plane).
2. Identify the crack center of the crack in the crack plane.
3. Construct radial lines embedded in the crack average plane and starting from the center of the crack.
4. Identify intersection between the lines and each crack front.
5. Utilize the intersection of each radial line with two subsequent crack fronts, compute dN and:
    a. compute their distance, or
    b. project the line connecting the subsequent crack front on the actual crack surface and then compute its total length.
6. Compute da/dN normalizing the result of Step 5 by dN.

Step 5(a) gives a first order approximation, which is reasonable when dealing with long cracks. Step 5(b) has been adopted by Herbig et al. (2011) and Spear et al. (2014), it accounts for the tortuosity of the crack surface, therefore increasing the fidelity of the reconstructed crack growth rate. The latter can be used when dealing with well-behaved small crack (e.g. no bifurcations and an almost ellipsoidal front).

A.2 Slip direction based reconstruction

At each location of the crack front the following algorithm is applied:

1. Identify the cycle number of the selected crack front (i.e. cn_i)
2. Identify the corresponding grain orientation and compute its available slip directions.
3. For each available slip direction (SD):
    a. Define a radial coordinate s starting at the crack front and aligned with SD
    b. Check that the selected SD is not pointing backward (i.e. is going behind the crack front). If this statement is true mark the SD as *available* and go to next step, else mark the SD as *not-available*
    c. Check that the SD is embedded in the crack plane (comparing with results of the macro feature tracking algorithm) and, if this is true then go to Step 3(d), else mark the direction as *non-failing*.
    d. Follow SD for a predetermined length l_0 with an imposed step length Δs.
    e. For each step record the failure cycle of the nearest crack surface facet (i.e. cn_j).
    f. Check that cn_j is ordered in an ascending manner (i.e. moving further from the crack front the cycle of failure keep increasing). If this is true go to the next step, else mark the SD as *non-failing*.

g. Compute the average FCGR along SD $\left(i.e. {d\vec{a}}/{dN} = {l_0}/{\left(\overline{cn_j} - cn_i\right)}\right)$ and mark SD as *possibly failing*.

4. Of all the directions marked as *possibly failing*, mark the one exhibiting the highest FCGR as *failing*.

In this work, $l_0 = 6.3\ \mu m$ and $\Delta s = 0.35\ \mu m$. The reason for choosing these parameters is explained in Section 3.1.

As a note, even though only 4 independents $\langle 11\bar{1} \rangle$ slip directions exist, the mining procedure needs to check 8 directions to account for the conjugate values. For example, given the $[1\bar{1}1]$ direction, its inverse, which is the $[\bar{1}1\bar{1}]$ needs to be checked.

Appendix B

Table 4 and Table 5 contain the edges of the discretization interval obtain by utilizing the genetic algorithm present in BayesiaLab.

Table 4: discretization intervals of continuous variable for BN^{FnF}

EDGE	1	2	3	4	5	6	7	8	9	10
DF(1)	-Inf	-9.473	-8.223	-7.131	-6.120	-5.249	-4.502	-3.634	-2.521	Inf
DF(2)	-Inf	-9.704	-8.498	-7.539	-6.638	-5.867	-5.107	-4.108	-2.700	Inf
DF(3)	-Inf	-10.093	-8.722	-7.646	-6.639	-5.831	-5.115	-4.065	-2.809	Inf
DF(4)	-Inf	-10.609	-9.161	-8.042	-7.035	-6.177	-5.285	-4.193	-3.015	Inf
DF(5)	-Inf	-10.914	-9.435	-8.322	-7.328	-6.462	-5.674	-4.798	-3.365	Inf
DF(6)	-Inf	-11.475	-9.855	-8.976	-7.838	-6.597	-5.753	-4.874	-3.418	Inf
DF(7)	-Inf	-12.402	-10.011	-9.064	-7.830	-6.602	-5.704	-4.771	-3.336	Inf
DF(8)	-Inf	-12.675	-10.368	-9.096	-7.902	-6.677	-5.902	-5.002	-3.520	Inf

Table 5: discretization intervals of continuous variable for BN^{GR}

EDGE	1	2	3	4	5	6	7	8	9	10	11
FCGR	-Inf	0.0003	0.0006	0.0011	0.0019	Inf					
DF(1)	-Inf	-8.028	-6.877	-6.100	-5.566	-5.055	-4.517	-3.845	-3.132	-2.316	Inf
DF(2)	-Inf	-8.099	-6.874	-6.202	-5.670	-5.203	-4.639	-4.038	-3.272	-2.330	Inf
DF(3)	-Inf	-8.489	-6.778	-6.116	-5.684	-5.200	-4.515	-3.611	-2.473	Inf	
DF(4)	-Inf	-8.665	-6.994	-6.385	-5.816	-5.285	-4.540	-3.614	-2.572	Inf	
DF(5)	-Inf	-8.830	-7.069	-6.492	-5.932	-5.453	-4.819	-3.889	-2.627	Inf	
DF(6)	-Inf	-8.797	-7.127	-6.588	-6.077	-5.704	-5.222	-4.261	-3.044	Inf	
DF(7)	-Inf	-8.928	-7.151	-6.660	-6.210	-5.875	-5.443	-4.833	-4.147	-2.936	Inf
DF(8)	-Inf	-8.956	-7.172	-6.620	-6.084	-5.617	-4.990	-4.188	-2.891	Inf	

Appendix C: Macro feature tracking algorithm

1. Divide the crack surface into grains, then for each grain
    a. A random facet is selected as seed point, its orientation is computed and the closest available slip plane is selected (minimizing the misorientation angle).
    b. Utilizing the adjacency matrix of the crack surface, facets in a small region surrounding the seed point are selected, their average orientation is computed, and assigned to the closest slip plane.
    c. If the slip plane assigned to the seed point is the same as the one assigned to its adjacent region (e.g. if the selected seed point belongs to a flat surface), then the selected seed region is marked as trustable (i.e. proceed to Step 1d), if not select a different seed point (i.e. go back to Step 1a).
    d. Construct an analytic representation of the assigned slip plane of failure utilizing: (i) the normal of the assigned plane of failure and (ii) the location of the trustable seed point. Also, record the slip directions available for the assigned slip plane.
    e. Identify facets neighboring the trustable seed region, and compute the distance between their barycenter and the analytic plane of failure. All the facets showing a distance smaller than an imposed threshold are marked as belonging to the assigned plane of failure, while the others are discarded.
    f. Repeat Step 1e until no more suitable neighboring facets can be found.
    g. Repeat Steps 1a-1f until the complete area of the crack surface belonging to the selected grain has been completely assigned, or no more trustable seed region can be found.
2. Repeat Step 1 for all the grains embedding the crack surface.

7 References

Acharya, A., 2007. Jump condition for GND evolution as a constraint on slip transmission at grain boundaries. Philos. Mag. 87, 1349–1359. doi:10.1080/14786430600951537

Acharya, A., Beaudoin, A.J., Miller, R., 2008. New Perspectives in Plasticity Theory: Dislocation Nucleation, Waves, and Partial Continuity of Plastic Strain Rate. Math. Mech. Solids 13, 292–315. doi:10.1177/1081286507086903

Bray, G.H., Glazov, M., Rioja, R.J., Li, D., Gangloff, R.P., 2001. Effect of artificial aging on the fatigue crack propagation resistance of 2000 series aluminum alloys. Int. J. Fatigue 23, 265–276. doi:10.1016/S0142-1123(01)00159-1

Buffiere, J.-Y.Y., Ferrie, E., Proudhon, H., Ludwig, W., 2006. Three-dimensional visualisation of fatigue cracks in metals using high resolution synchrotron X-ray micro-tomography. Mater. Sci. Technol. 22, 1019–1024. doi:10.1179/174328406X114135

Castelluccio, G.M., McDowell, D.L., 2015. Microstructure and mesh sensitivities of mesoscale surrogate driving force measures for transgranular fatigue cracks in polycrystals. Mater. Sci. Eng. A 639, 626–639. doi:10.1016/j.msea.2015.05.048

Castelluccio, G.M., McDowell, D.L., 2014. A mesoscale approach for growth of 3D microstructurally small fatigue cracks in polycrystals. Int. J. Damage Mech. 23, 791–818. doi:10.1177/1056789513513916

Castelluccio, G.M., McDowell, D.L., 2012. Assessment of small fatigue crack growth driving forces in single crystals with and without slip bands. Int. J. Fract. 176, 49–64. doi:10.1007/s10704-012-9726-y

Castelluccio, G.M., Musinski, W.D., McDowell, D.L., 2016. Computational Micromechanics of Fatigue of Microstructures in the HCF-VHCF Regimes. Int. J. Fatigue. doi:10.1016/j.ijfatigue.2016.05.019

Cerrone, A., Stein, C., Pokharel, R., Hefferan, C., Lind, J., Tucker, H., Suter, R.M., Rollett, A.D., Ingraffea, A.R., 2015. Implementation and verification of a microstructure-based capability for modeling microcrack nucleation in LSHR at room temperature. Model. Simul. Mater. Sci. Eng. 23, 35006. doi:10.1088/0965-0393/23/3/035006

Correa, C.D., Lindstrom, P., 2013. the Mutual Information Diagram for Uncertainty Visualization. Int. J. Uncertain. Quantif. 3, 187–201. doi:10.1615/Int.J.UncertaintyQuantification.2012003959

Davidson, D.L., Chan, K., McClung, R., Hudak, S., 2003. Small Fatigue Cracks, in: Comprehensive Structural Integrity. Elsevier, pp. 129–164. doi:10.1016/B0-08-043749-4/04073-8

Devincre, B., Roberts, S.G., 1996. Three-Dimensional simulation of dislocation-crack interactions in b.c.c. metals at the mesoscopic scale. Acta Mater. 44, 2891–2900. doi:10.1016/1359-6454(95)00411-4

Fatemi, A., Socie, D.F., 1988. A critical plane approach to multiaxial fatigue damage including out-of-phase loading. Fatigue Fract. Eng. Mater. Struct. 11, 149–165. doi:10.1111/j.1460-2695.1988.tb01169.x

Fréour, S., Lacoste, E., François, M., Guillén, R., 2011. Determining Ti-17 β-Phase Single-Crystal Elasticity Constants through X-Ray Diffraction and Inverse Scale Transition Model. Mater. Sci. Forum 681, 97–102. doi:10.4028/www.scientific.net/MSF.681.97

Friedman, N., Geiger, D., Goldszmidt, M., 1997. Bayesian Network Classifier. Mach. Learn. 29, 131–163. doi:10.1023/A:1007465528199

George, A., Michot, G., 1993. Dislocation loops at crack tips: nucleation and growth— an

experimental study in silicon. Mater. Sci. Eng. A 164, 118–134. doi:10.1016/0921-5093(93)90649-Y
Gibson, M.A., Forwood, C.T., 2002. Slip transfer of deformation twins in duplex ??-based Ti-Al alloys part III. Transfer across general large-angle ??-?? grain boundaries. Philos. Mag. A Phys. Condens. Matter, Struct. Defects Mech. Prop. 82, 1381–1404. doi:10.1080/01418610208235678
Gilormini, P., Bacroix, B., Jonas, J.J., 1988. Theoretical analyses of 〈111〉 pencil glide in b.c.c. crystals. Acta Metall. 36, 231–256. doi:10.1016/0001-6160(88)90001-6
Harren, S., Lowe, T.C., Asaro, R.J., Needleman, A., 1989. Analysis of Large-Strain Shear in Rate-Dependent Face-Centred Cubic Polycrystals: Correlation of Micro- and Macromechanics. Philos. Trans. R. Soc. A Math. Phys. Eng. Sci. 328, 443–500. doi:10.1098/rsta.1989.0048
Herbig, M., King, A., Reischig, P., Proudhon, H., Lauridsen, E.M., Marrow, J., Buffière, J.-Y., Ludwig, W., 2011. 3-D growth of a short fatigue crack within a polycrystalline microstructure studied using combined diffraction and phase-contrast X-ray tomography. Acta Mater. 59, 590–601. doi:10.1016/j.actamat.2010.09.063
Hochhalter, J.D., Littlewood, D.J., Veilleux, M.G., Bozek, J.E., Maniatty, A.M., Rollett, A.D., Ingraffea, A.R., 2011. A geometric approach to modeling microstructurally small fatigue crack formation: III. Development of a semi-empirical model for nucleation. Model. Simul. Mater. Sci. Eng. 19, 35008. doi:10.1088/0965-0393/19/3/035008
Hull, D., Bacon, D.J., 2011. Introduction to dislocations. Butterworth-Heinemann.
Hutchinson, J.W., 1977. Creep and plasticity of hexagonal polycrystals as related to single crystal slip. Metall. Mater. Trans. A 8, 1465–1469.
Kocks, U.F., 1970. The relation between polycrystal deformation and single-crystal deformation. Metall. Mater. Trans. 1, 1121–1143. doi:10.1007/BF02900224
Lebensohn, R.A., Kanjarla, A.K., Eisenlohr, P., 2012. An elasto-viscoplastic formulation based on fast Fourier transforms for the prediction of micromechanical fields in polycrystalline materials. Int. J. Plast. 32–33, 59–69. doi:10.1016/j.ijplas.2011.12.005
Lee, T.C., Robertson, I.M., Birnbaum, H.K., 1989. Prediction of slip transfer mechanisms across grain boundaries. Scr. Metall. 23, 799–803. doi:10.1016/0036-9748(89)90534-6
Li, J., Proudhon, H., Roos, A., Chiaruttini, V., Forest, S., 2014. Crystal plasticity finite element simulation of crack growth in single crystals. Comput. Mater. Sci. 94, 191–197. doi:10.1016/j.commatsci.2014.03.061
Lieberman, E.J., Rollett, A.D., Lebensohn, R.A., Kober, E.M., 2015. Calculation of grain boundary normals directly from 3D microstructure images. Model. Simul. Mater. Sci. Eng. 23, 35005. doi:10.1088/0965-0393/23/3/035005
Livingston, J.D., Chalmers, B., 1957. Multiple slip in bicrystal deformation. Acta Metall. 5, 322–327. doi:10.1016/0001-6160(57)90044-5
Luster, J., Morris, M.A., 1995. Compatibility of deformation in two-phase Ti-Al alloys: Dependence on microstructure and orientation relationships. Metall. Mater. Trans. A 26, 1745–1756. doi:10.1007/BF02670762
Mach, J.C., Beaudoin, A.J., Acharya, A., 2010. Continuity in the plastic strain rate and its influence on texture evolution. J. Mech. Phys. Solids 58, 105–128. doi:10.1016/j.jmps.2009.11.005
Metropolis, N., Rosenbluth, A.W., Rosenbluth, M.N., Teller, A.H., Teller, E., 1953. Equation of state calculations by fast computing machines. J. Chem. Phys. 21, 1087–1092.

doi:http://dx.doi.org/10.1063/1.1699114
Metropolis, N., Ulam, S., 1949. The Monte Carlo Method. J. Am. Stat. Assoc. 44, 335. doi:10.2307/2280232
Musinski, W.D., McDowell, D.L., 2016. Simulating the effect of grain boundaries on microstructurally small fatigue crack growth from a focused ion beam notch through a three-dimensional array of grains. Acta Mater. 112, 20–39. doi:10.1016/j.actamat.2016.04.006
Neumann, P., 1974a. New experiments concerning the slip processes at propagating fatigue cracks—I. Acta Metall. 22, 1155–1165. doi:10.1016/0001-6160(74)90071-6
Neumann, P., 1974b. The geometry of slip processes at a propagating fatigue crack—II. Acta Metall. 22, 1167–1178. doi:10.1016/0001-6160(74)90072-8
Neumann, P., 1969. Coarse slip model of fatigue. Acta Metall. 17, 1219–1225. doi:10.1016/0001-6160(69)90099-6
Paris, P.C., Gomez, M.P., Anderson, W.E., 1961. A rational analytic theory of fatigue. trend Eng. 13, 9–14.
Pearl, J., 1985. Bayesian Networks A Model of Self-Activated Memory for Evidential Reasoning, in: Proceedings of the 7th Conference of the Cognitive Science Society. doi:citeulike-article-id:3847802
Pearson, K., 1895. Note on Regression and Inheritance in the Case of Two Parents. Proc. R. Soc. London 58, 240–242.
Proudhon, H., Li, J., Ludwig, W., Roos, A., Forest, S., 2017. Simulation of Short Fatigue Crack Propagation in a 3D Experimental Microstructure. Adv. Eng. Mater. 19, 1600721. doi:10.1002/adem.201600721
Proudhon, H., Li, J., Wang, F., Roos, a., Chiaruttini, V., Forest, S., 2015. 3D simulation of short fatigue crack propagation by finite element crystal plasticity and remeshing. Int. J. Fatigue 82, 1–9. doi:10.1016/j.ijfatigue.2015.05.022
Rovinelli, A., Lebensohn, R.A., Sangid, M.D., 2015. Influence of microstructure variability on short crack behavior through postulated micromechanical short crack driving force metrics. Eng. Fract. Mech. 138, 265–288. doi:10.1016/j.engfracmech.2015.03.001
Rovinelli, A., Proudhon, H., Lebensohn, R.A., Sangid, M.D., 2017a. Assessing the Reliability of Fast Fourier Transformation Based Crystal Plasticity Simulations of a Polycrystalline Material near a Crack Tip. Submitted, under review.
Rovinelli, A., Sangid, M.D., Proudhon, H., Guilhem, Y., Lebensohn, R.A., Ludwig, W., 2017b. Assessing reliability of fatigue indicator parameters for small crack growth via a probabilistic framework. Model. Simul. Mater. Sci. Eng. 25, 45010. doi:10.1088/1361-651X/aa6c45
Sangid, M.D., Ezaz, T., Sehitoglu, H., Robertson, I.M., 2011. Energy of slip transmission and nucleation at grain boundaries. Acta Mater. 59, 283–296. doi:10.1016/j.actamat.2010.09.032
Schäf, W., Marx, M., Knorr, A.F., 2013. Influence of microstructural barriers on small fatigue crack growth in mild steel. Int. J. Fatigue 57, 86–92. doi:10.1016/j.ijfatigue.2012.11.006
Schäf, W., Marx, M., Vehoff, H., Heckl, A., Randelzhofer, P., 2011. A 3-D view on the mechanisms of short fatigue cracks interacting with grain boundaries. Acta Mater. 59, 1849–1861. doi:10.1016/j.actamat.2010.11.051
Schäfer, F., Weiter, L., Marx, M., Motz, C., 2016. Quantifying the grain boundary resistance against slip transfer by experimental combination of geometric and stress approach using

stage-I-fatigue cracks. Philos. Mag. 96, 3524–3551. doi:10.1080/14786435.2016.1235289
Schijve, J., 2009. Fatigue of Structures and Materials, 2nd ed, Journal of Chemical Information and Modeling. Springer Netherlands, Dordrecht. doi:10.1007/978-1-4020-6808-9
Shannon, C.E., Weaver, W., 1949. The mathematical theory of information.
Shen, Z., Wagoner, R.H., Clark, W.A.T., 1986. Dislocation pile-up and grain boundary interactions in 304 stainless steel. Scr. Metall. 20, 921–926. doi:10.1016/0036-9748(86)90467-9
Spear, A.D., Li, S.F., Lind, J.F., Suter, R.M., Ingraffea, A.R., 2014. Three-dimensional characterization of microstructurally small fatigue-crack evolution using quantitative fractography combined with post-mortem X-ray tomography and high-energy X-ray diffraction microscopy. Acta Mater. 76, 413–424. doi:10.1016/j.actamat.2014.05.021
Taylor, G.I., Elam, C.F., 1926. The Distortion of Iron Crystals. Proc. R. Soc. London. Ser. A, Contain. Pap. a Math. Phys. Character 112, 337–361.
Vehoff, H., Neumann, P., 1979. In situ sem experiments concerning the mechanism of ductile crack growth. Acta Metall. 27, 915–920. doi:10.1016/0001-6160(79)90126-3
Weinberger, C.R., Boyce, B.L., Battaile, C.C., 2013. Slip planes in bcc transition metals. Int. Mater. Rev. 58, 296–314. doi:10.1179/1743280412Y.0000000015
Yeratapally, S.R., Glavicic, M.G., Argyrakis, C., Sangid, M.D., 2017. Bayesian uncertainty quantification and propagation for validation of a microstructure sensitive model for prediction of fatigue crack initiation. Reliab. Eng. Syst. Saf. 164, 110–123. doi:10.1016/j.ress.2017.03.006
Yeratapally, S.R., Glavicic, M.G., Hardy, M., Sangid, M.D., 2016. Microstructure based fatigue life prediction framework for polycrystalline nickel-base superalloys with emphasis on the role played by twin boundaries in crack initiation. Acta Mater. 107, 152–167. doi:10.1016/j.actamat.2016.01.038
Zhai, T., Jiang, X., Li, J., Garratt, M., Bray, G., 2005. The grain boundary geometry for optimum resistance to growth of short fatigue cracks in high strength Al-alloys. Int. J. Fatigue 27, 1202–1209. doi:10.1016/j.ijfatigue.2005.06.021
Zhai, T., Wilkinson, A.J., Martin, J.W., 2000. A crystallographic mechanism for fatigue crack propagation through grain boundaries. Acta Mater. 48, 4917–4927. doi:10.1016/S1359-6454(00)00214-7
Zhang, Y.H., Edwards, L., 1992. The effect of grain boundaries on the development of plastic deformation ahead of small fatigue cracks. Scr. Metall. Mater. 26, 1901–1906. doi:10.1016/0956-716X(92)90056-K